Insights into the Benzodihydrofuran Derivative-Induced Conformational and Structural Changes in the Alzheimer's Disease-Associated Amyloid-β Peptide

A

Dissertation Submitted

in partial fulfillment of the requirements for the degree of

Master of Science

in

Chemistry

By

Ashish Kumar

(Reg. No. 302302007)

Under the guidance of

Dr. Bhupesh Goyal

THAPAR INSTITUTE
OF ENGINEERING & TECHNOLOGY
(Deemed to be University)

DEPARTMENT OF CHEMISTRY AND BIOCHEMISTRY

THAPAR INSTITUTE OF ENGINEERING AND TECHNOLOGY, PATIALA–147004

JUNE 30, 2025

DECLARATION

I hereby declare that the dissertation entitled "***Insights into the benzodihydrofuran derivative-induced conformational and structural changes in the Alzheimer's disease-associated amyloid-β peptide***" presented in partial fulfilment of the requirements for the award of the degree of **Master of Science in Chemistry** to **Department of Chemistry and Biochemistry, Thapar Institute of Engineering and Technology, Patiala, Punjab** is a record of the independent research conducted by me from January to June 2025 under the guidance of Dr. Bhupesh Goyal. The information derived from the literature has been duly acknowledged in the text and a list of references is provided. Additionally, none of the components of this dissertation have been submitted to another university for consideration of a different degree or diploma.

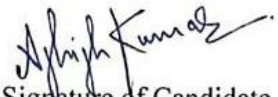

Signature of Candidate

Date: 30th June, 2025

Ashish Kumar

Place: TIET, Patiala

Regn. No. 302302007

CERTIFICATE

This is to certify that the dissertation entitled "***Insights into the benzodihydrofuran derivative-induced conformational and structural changes in the Alzheimer's disease-associated amyloid-β peptide***" submitted by **Mr. Ashish Kumar** to **Department of Chemistry and Biochemistry, Thapar Institute of Engineering and Technology, Patiala, Punjab** in partial fulfilment of the requirements for the award of the degree of **Master of Science in Chemistry**, is an authentic record of the work carried out by the candidate under my/our guidance and supervision. He has fulfilled the requirements for the submission of this dissertation, which to my knowledge has reached the requisite standard. The results embodied in the dissertation have not been submitted in part or full to any other University or Institute for the award of any other degree or diploma.

Date: 30th June, 2025

Place: TIET, Patiala

Bhupesh Goyal

Signature 30/06/2025

Dr. Bhupesh Goyal

Associate Professor

Department of Chemistry and Biochemistry

ACKNOWLEDGEMENT

Firstly, I offer my deepest gratitude to the Almighty for his infinite blessings, wisdom, and the opportunities that allowed me to complete this dissertation successfully. I am also immensely grateful to Dr. Manmohan Chhibber, Professor and Head of the Department of Chemistry and Biochemistry, for providing me with the opportunity to explore the field of research through this work.

I extend my sincere thanks to my supervisor, Dr. Bhupesh Goyal, for his outstanding guidance, expertise, and continuous support throughout this research journey. His valuable insights and constructive feedback have played a pivotal role in shaping this thesis, and I remain deeply grateful for his mentorship.

I am also truly thankful to my mentor, Ms. Diksha, for her constant guidance and supervision during the entire course of my project. Her instructions in research methodologies and her unwavering encouragement have been of immense help to me. Furthermore, I am very grateful to the research scholars in my lab Ms. Arushi, Ms. Gurmeet, Ms. Tanishka, Mr. Ishwar, and Ms. Jahanvi, for their inspiring guidance, cooperation, and support throughout this research work.

My deepest thanks go to the Thapar Institute of Engineering and Technology (TIET) for providing the essential facilities and infrastructure for this study.

In conclusion, the completion of this thesis is the result of collaborative efforts and support of an exceptional network of individuals, for which I am genuinely thankful.

Thank you all.
Date: 30th June, 2025
Place: TIET, Patiala

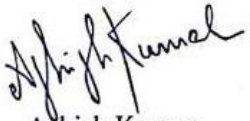

Ashish Kumar

ABSTRACT

The progression of Alzheimer's disease (AD) is linked to the misfolding and aggregation of amyloid−β (Aβ) monomers into neurotoxic soluble oligomers, protofibrils, and ultimately mature fibrils. The most effective therapeutic approach for treating AD is to inhibit $A\beta_{42}$ aggregation. Metal complexes and small molecules have been identified as promising inhibitors to combat self–aggregation of $A\beta_{42}$ monomer. A binuclear metal complex PtRu–1($[Ru(bpy)_2(dpp)PtCl_2]Cl_2$**)**, containing Pt^{II} and Ru^{II} metal centers, has been previously reported to inhibit the $A\beta_{42}$ aggregation in early stages. Thioflavin–T (ThT) assay revealed that incubation of $A\beta_{42}$ with equimolar or 2−fold molar excess of PtRu–1 led to a 90% decrease in ThT fluorescence, highlighting inhibitory potential against $A\beta_{42}$ aggregation. Despite comprehensive experimental investigations, the molecular interactions and binding mechanism underlying the inhibitory capacity of Pt−Ru1 on $A\beta_{42}$ aggregation remain unidentified. Thus, an attempt was made to examine the molecular mechanism by which Pt−Ru1 inhibits the aggregation of $A\beta_{42}$ monomer. The molecular docking results depict favourable binding (–6.45 kcal/mol) of Pt−Ru1 to $A\beta_{42}$ monomer influenced by hydrogen bonds, hydrophobic contacts, and π−π stacking interactions.

Sánchez et al. synthesized 15 chalcone derivatives using Claisen–Schmidt condensation by utilizing a natural benzodihydrofuran compound, *i.e.*, fomannoxine. Fluorine substitution was found to significantly enhance cytoprotective activity and reduce the aggregation rate of Aβ, making them promising therapeutic candidates. ThT fluorescence analysis reveals that co-incubation of chalcone−3c with Aβ led to a reduction in fluorescence intensity. Notably, chalcone−3c enhanced cell viability by 50%, thereby reducing cytotoxicity and showing no cytotoxic effect at different concentrations. Thus, molecular docking as well as molecular dynamics (MD) simulations were employed to examine the inhibitory mechanism of chalcone3c against self–aggregation of $A\beta_{42}$ monomer. The molecular docking results indicated a favorable interaction of chalcone−3c with the $A\beta_{42}$ monomer, exhibiting a binding energy of −6.7 kcal/mol. The RMSD and RMSF evaluations exhibited a decrease in conformational variations in the $A\beta_{42}$ monomer following the inclusion of chalcone−3c. An increase in helix content was detected in the $A\beta_{42}$ monomer, rising from 20.2 ± 1.6 % to 33.8 ± 1.5 %, indicating a reduction in the aggregation tendency of the $A\beta_{42}$ monomer in the presence of chalcone−3c. Additionally, the intramolecular hydrogen bonds rise from 21.37 ± 0.96 to 22.19 ± 1.05 with the addition of

chalcone−3c, supporting the enhancement of the helical conformation of $A\beta_{42}$ monomer. Contact map analysis revealed reduced aggregation tendency of $A\beta_{42}$ monomer on the incorporation of chalcone−3c due to reduction in residue interaction in the central hydrophobic core (CHC) and C−terminal region. PCA, FEL, and conformational clustering studies highlight higher conformational homogeneity in $A\beta_{42}$ monomer in the presence of chalcone−3c, which indicates lower fibrillation propensity in $A\beta_{42}$ monomer. The illumination of the molecular interactions between $A\beta_{42}$ monomer and chalcone−3c provides critical insights for the strategic development of more effective aggregation inhibitors as prospective therapeutic candidates against Aβ aggregation in AD.

TABLE OF CONTENTS

LIST OF TABLES

LIST OF FIGURES

LIST OF ABBREVIATIONS

Abbreviations	Full meaning/name
AD	Alzheimer's Disease
PD	Parkinson's Disease
FDA	Food and Drug Administration
AChE	Acetylcholinesterase
NMDA	N–methyl–D aspartate
Aβ	Amyloid–beta
ROS	Reactive Oxygen Species
APP	Amyloid Precursor Protein
CTF β	C–Terminal Fragment β
AICD	Amyloid Intracellular Domain
WHO	World Health Organization
BBB	Blood–Brain Barrier
DNA	Deoxyribonucleic Acid
ThT	Thioflavin–T
SDS–PAGE	Sodium Dodecyl Sulfate Polyacrylamide Gel Electrophoresis
DFT	Density Functional Theory
SEC	Size Exclusion Chromatography
TEM	Transmission Electron Microscopy
NMR	Nuclear Magnetic Resonance
CAS	Catalytic Active Sites
PAS	Peripheral Anionic Sites
ESI–MS	Electrospray Ionization Mass Spectrometry
SARs	Structure–Activity Relationships
DLS	Dynamic Light Scattering
SOD	Superoxide Dismutase
MD	Molecular Dynamics
GDP	Gabapentin
Cin	Cinnamaldehyde
PEA	Phenylethyl alcohol
ASA	α–Asarone
BCP	β–Caryophyllene
ANS	8–Anilino–1–naphthalenesulfonic acid fluorescence
Far–UV CD	Far–Ultraviolet Circular Dichroism
RMSD	Root Mean Square Deviation
R_g	Radius of Gyration
MM–GSBA	Molecular Mechanics Generalized Born Surface Area
MM–PBSA	Molecular Mechanics Poisson-Boltzmann Surface Area

ADMET	Absorption, Distribution, Metabolism, Excretion, and Toxicity
BuChE	Butyrylcholinesterase
WGalNAc	Tryptophan–Galactosylamine Conjugate
LGA	Lamarckian Genetic Algorithm
RCSB	Research Collaboratory for Structural Bioinformatics
PDB	Protein Data Bank
ATB	Automated Topology Builder
PME	Particle Mesh Ewald
FEL	Free Energy Landscape
PCA	Principal Component Analysis
MCPB	Metal Center Parameter Builder
CHC	Central Hydrophobic Core

CHAPTER 1: Introduction

Protein comprises of series of different amino acids that are crucial for the formation of enzymes, muscles, bones, and hormones.[1] Protein folds into its native 3D structure for various biological functions in the body. Protein that fails to fold into its 3D structure due to mutation, pH change, or temperature change, leads to misfolding, thereby losing its functionality. Many disorders, including Alzheimer's disease (AD), Parkinson's disease (PD), Huntington's disease, and other neurological diseases, are caused by the aggregation of misfolded proteins as they expose the hydrophobic region outside and encourage intermolecular interactions.[2] According to the World Health Organization (WHO), the number of citizens suffering from dementia worldwide is estimated to increase from 55 million in 2019 to 139 million by the year 2050.[3] The estimated dementia rate for adults aged 60+ in India is 7.4%. About 8.8 million Indians older than 60 years live with dementia. Although the Food and Drug Administration (FDA) has approved some drugs: donepezil, galantamine, memantine, and suvorexant targeting acetylcholinesterase (AChE) and N–methyl–D aspartate (NMDA) receptor, giving only symptomatic relief against AD.[4] Therefore, it is a relevant target for research purposes due to the unavailability of its treatment.

The pathogenesis of AD is defined by various factors that include: accumulation of fibrillar aggregates of Aβ,[5] metal ion dyshomeostasis,[6] reactive oxygen species (ROS),[7] and dysfunction of autophagy.[8] Amyloid precursor protein (APP) is a transmembrane protein, cleaved by two different pathways: amyloidogenic and non–amyloidogenic.[9] In the non–amyloidogenic pathway, APP is first cleaved by α–secretase, followed by γ–secretase, leading to soluble and non–toxic APP–α form. In the amyloidogenic pathway, it leads to cleavage of APP protein via β secretase, followed by γ secretase, leading to the formation of Aβ, which aggregates into a toxic form. The β–Secretase/BACE1 enzyme cleaves APP to a soluble APP–β fragment and a C–terminal fragment β (CTFβ), having a full–length Aβ peptide at the N–terminal. CTFβ is cleaved by γ–secretase to give the amyloid intracellular domain (AICD) fragment, i.e., $A\beta_{1-40/42}$ fragment.[10] γ–Secretase, as a multiprotease complex, generates Aβ peptides of varying lengths, with $A\beta_{42}$ and $A\beta_{40}$ being the most prevalent forms in plaques, out of which $A\beta_{40}$ is most abundant; however, $A\beta_{42}$ exhibits more aggregation and toxicity.[11] Hence, $A\beta_{42}$ is of greater significance to work upon. The hydrophobic residues of the Aβ peptide aggregate to evade

contact with water, which facilitates interactions among the hydrophobic side chains, forming stable non–covalent interactions. These interactions are the primary driving force for Aβ aggregation.[12]

Additionally, Metal ions are known to play a crucial role in various cellular activities including neural synaptic activity, modulating the blood–brain barrier (BBB) and facilitating the operation of certain metalloproteins, such as Cu/Zn superoxide dismutase (SOD) within the brain.[13] The metal ion hypothesis speculates that dyshomeostasis and the disproportion of metal ions contribute to the pathology of AD.[8] Metal ions, especially Cu^{2+} was found to form complexes with $A\beta_{42}$, resulting in the generation of more neurotoxic aggregates than $A\beta_{42}$ in isolation.[8] Cu^{2+} ions contribute to the formation of ROS through complex formation with $A\beta_{42}$, resulting in oxidative stress that causes neuronal damage.[14]

Recently, the "one compound−multitarget approach" has been introduced as a novel method for drug development, which takes into consideration the complex character of AD.[15] The development of multifunctional drugs that are capable of targeting multiple pathologies of AD simultaneously could be a useful strategy for its treatment. [16] In recent decades, researchers have developed several inhibitors, including metal chelators,[17] peptidomimetics,[18] alkaloids,[19] terpenoids,[20] and glycosides,[21] metal coordination complex,[22] and small molecules,[23] for the treatment of AD. Transition metal complexes prevent $A\beta_{42}$ aggregation *via* three pathways:[24] (i) Hydrolytic cleavage of the peptide bond in the protein. (ii) Oxidative modification of metal complexes generates ROS that oxidize residues like histidine, methionine, and tyrosine in $A\beta_{42}$ and hence prevent self–aggregation. (iii) Direct coordination of the $A\beta_{42}$, metal complex directly binds to specific amino acids and hence blocks aggregation sites. He et al. reported $[VO(O_2)_2(bipy)]$ metal complex as the inhibitor of $A\beta_{42}$ aggregation by oxidation of methionine, and hence disrupts the hydrophobic interaction required for fibril stabilization.[25] Ma et al. reported the first metallo–therapeutic compound [Pt(1,10–phenanthroline)Cl_2] for AD therapy, where Pt(II) binds to imidazole groups present in His6, His14 of $A\beta_{42}$ monomer and disrupts the electrostatic interactions between adjacent $A\beta_{42}$ molecules and hence prevents aggregation.[26] Cohen et al. reported that platinum(II) complex cisplatin (cis–$[Pt(NH_3)_2Cl_2]$) has been employed as a pharmaceutical intercalator of deoxyribonucleic acid (DNA) utilized in chemotherapy.[27] Kumar et al. examined the inhibitory effectiveness of a novel binuclear metal complex, $[(bpy)_2Ru(II)(dpp)Pt(II)Cl_2]Cl_2$ (PtRu–1) on $A\beta_{42}$ peptide aggregation[28] and contrasted it with a

previously reported platinum–based complex, [Pt(BPS)Cl_2] (Pt–1).[29] ThT fluorescence assay demonstrated that PtRu–1 prevented $A\beta_{42}$ aggregation by decreasing fluorescence by ~90% at equimolar or 2–fold molar excess. The computational binding energy calculated using density functional theory (DFT)–based method revealed that PtRu–1 binds to both histidine and N–terminal residues of $A\beta_{42}$, suggesting improved binding potential attributed to the presence of Ru(II). Mass spectrometry revealed stoichiometric binding of PtRu–1 to $A\beta_{42}$ with the molar ratio of 1:1 and 1:2. Overall, PtRu–1 suppressed $A\beta_{42}$ self–aggregation and inhibited formation of harmful oligomers, underscoring the promise of multi–metallic complexes as therapeutic treatment for AD. Thus, an attempt to identify the underlying mechanism behind the inhibitory mechanism of PtRu–1 against self–aggregation of $A\beta_{42}$ monomer was made.

Apart from metal complexes as inhibitors, small molecules[23] exhibit a tendency to inhibit aggregation through several processes, including restriction of APP cleavage, destabilizing existing aggregates, and inhibiting $A\beta_{42}$ monomer aggregation.[30] Small-molecule inhibitors possess great inhibitory potential due to their permeability across the BBB, immunological tolerance, and stability in biological fluids.[31] Small-molecule inhibitors such as chalcones derived from natural benzodihydrofuran compounds have the potential to inhibit self–aggregation of $A\beta_{42}$.[32] Sánchez et al. synthesized and evaluated fifteen benzodihydrofuran–derived chalcones as promising therapeutic agents aimed at inhibiting $A\beta_{42}$ peptide aggregation, against AD.[32] Compounds 3c, 3d, and 3g displayed considerable cytoprotective properties in PC–12 neuronal cells among the other molecules. In the presence of $A\beta_{42}$, chalcone–3c ($C_{17}H_{13}FO_2$), which possesses a 3–fluorophenyl substitution, demonstrated a significant neuroprotective potential by recovering cell viability by 50 ± 6% at 300 nM and around 38% at 3 and 100 nM, restoring cell viability by over 60%. Aggregation tests with ThT fluorescence demonstrated that these chalcones influence $A\beta_{42}$ fibril development, with compound 3c significantly modifying the aggregation kinetics and reducing fibril formation. *In silico* docking investigations validated stable contacts between the active chalcones and two conformers of $A\beta_{42}$ monomer (1AML and 1IYT), revealing binding energies that ranged from −7.0 to −5.7 kcal/mol. The findings indicate that the compound interacts directly with $A\beta_{42}$, either stabilizing non-aggregating forms or inhibiting initial nucleation activities. Thus, the inhibitory mechanism of chalcone–3c was explored using molecular docking and MD simulations.

CHAPTER 2: Literature review

2.1. Literature review of metal complex (PtRu–1)

Table 1. Metal complex inhibitors of $A\beta_{42}$ aggregation.

S. No.	Metal complex	Key findings	References
1.	Ruthenium(II)–arene complex: RuBA [Ru(η^6–*p*–cymene)(4,4′–diamino–2,2′–bipyridine)Cl]PF_6]	• Design and synthesized a series of ruthenium (II)–arene complexes bearing substituted 2,2'–bipyridine ligands for $A\beta_{40}$ aggregation. • Inhibitory potential of RuBA against$A\beta_{40}$ aggregation was evaluated using ThT fluorescence, DLS, and transmission electron microscopy (TEM) techniques. • ThT assay showed RuBA reduced aggregation to 1.3% ± 0.9% compared to $A\beta_{40}$ alone, indicating strong suppression of fibril formation. • TEM revealed highly dispersed and less dense Aβ particles, and dynamic light scattering (DLS) confirmed smaller hydrodynamic radii (~231 nm), indicating inhibition of Aβ aggregation. • Nuclear magnetic resonance (NMR) studies show ligand exchange and strong interaction with imidazole groups and supported interaction of RuBA with histidine residues (His6, His13, His14) in Aβ. • MTT assay on PC–12 and C6 glioma cells showed low toxicity and high biocompatibility of RuBA at concentrations up to 40 μM. • RuBA outscored other Ru complexes, demonstrating that the structure–activity relationship underscored the significance of the amino groups on the bpy for anti–Aβ activity.	Hacker et al.[33]
2.	Heterometallic Ruthenium(II)–Platinum(II) complexes (3, 4)	• Two heteronuclear Ru(II)–Pt(II) complexes, $[Ru(bpy)_2(BPIMBp)PtCl_2]^{2+}$ (3) and $[Ru(phen)_2(BPIMBp)PtCl_2]^{2+}$ (4), were designed as dual–target agents for AChE inhibition and Aβ aggregation.	Vyas et al.[34]

	[Ru $(bpy)_2(BPIMBp)PtCl_2]^{2+}$ (3) & $[Ru(phen)_2(BPIMBp)PtCl_2]^{2+}$(4) (bpy= 2,2–bipyridine, phen = 1,10–phenanthroline, and BPIMBp = 1,4′–bis[(2–pyridin–2–yl)–1H–imidazol–1–ylmethyl]–1,1′–bipheny)	• Both complexes showed mixed/uncompetitive inhibition of AChE with IC_{50} values of 0.26 μM and 0.18 μM for complexes 3 and 4, respectively, indicating submicromolar potency and nearly 50–fold greater inhibition than $[Ru(phen)_3]^{2+}$. • DFT was used to optimize complex and molecular docking showed dual binding of complexes at the catalytic active (CAS) and peripheral anionic (PAS) sites of AChE (PDB: 1QTI). • Complexes 3 and 4 inhibited $A\beta_{1–40}$ aggregation up to 80% (70%inhibition to write) as shown by ThT fluorescence, turbidity assays, and confocal microscopy. • Electrospray ionization mass spectrometry (ESI–MS) and ^1H NMR confirmed covalent coordination to $A\beta_{1–16}$ via platinum center. • Cytotoxicity assays in SH–SY5Y cells showed moderate toxicity for complexes, and also suppressed Cu(II)–induced Aβ oxidation and ROS formation. • Complexes showed strong dual inhibition, decreasing AChE activity by as much as 80% and markedly inhibiting Aβ aggregation *in vitro*.	
3.	Ru–P9 (4–Aminopyridinium [trans–$RuCl_4$ (DMSO–S) (4–aminopyridine)	• Eleven Ru(III) complexes with varied 4–substituted pyridine ligands were synthesized to investigate structure–activity relationships (SARs) in Aβ aggregation inhibition. • Complexes Ru–P8 and Ru–P9, containing primary amine groups, significantly reduced $A\beta_{1–40}$ aggregation as confirmed by turbidity, DLS, and TEM assays. • Ru complexes show histidine–based coordination with $A\beta_{1–15}$, reducing cytotoxicity of Aβ in glioma cells from 64.8% to 83.0% viability, with Ru–P9 offering greater protection and affecting NMR peaks associated with His residues, indicating	Wall et al.[35]

		direct binding. • DLS data showed particle size reduction from 487.3 nm (Aβ alone) to as low as 122 nm in the presence of Ru–P6, confirming aggregation inhibition. Ru–P9 reduced the hydrodynamic diameter of Aβ aggregates to ~205.9 nm as shown by DLS analysis. • TEM images revealed Ru–P8, Ru–P9, and Ru–P10 produced the smallest and least dense aggregates. • SAR analysis emphasized the importance of hydrogen bond donors (especially $–NH_2$) over –OH groups for efficacy. • Complexes containing pyridine–based ligands have anti–Alzheimer's efficacy, whereas strong hydrogen bonding was linked to more AChE inhibition (up to 75%) and less Aβ aggregation.	
4.	Ruthenium (II) polypyridyl complexes (1, 2) Complex 1: $[Ru(phen)_3]^{2+}$, Complex 2: $[Ru(phen)_2(bxbg)]^{2+}$ (Phen = 1,10 phenanthroline, bxbg = bis (o–xylene) bipyridine glycoluril)	• Two complexes, $[Ru(phen)_3]^{2+}$ (1) and $[Ru(phen)_2(bxbg)]^{2+}$ (2), were studied for dual inhibition of AChE and $Aβ_{1–40}$ aggregation. • Complex 2 showed significantly higher AChE inhibition with IC_{50} = 0.30 ± 0.02 μM and Ki = 0.04 μM, which is 30 times more effective than other complex. • Molecular docking was used to AChE structure (PDB: 1QTI) and determine the binding orientation of complexes. • MD simulations confirmed stable positioning of complex 2 and revealed that it interacts with CAS and PAS, and mid–gorge sites of AChE, confirming multi–site engagement and stability. • Complex 2 completely prevented $Aβ_{1–40}$ aggregation up to 200 h, as shown by ThT fluorescence and TEM, while complex 1 only delayed aggregation. • Cytotoxicity assays on SH–SY5Y cells showed >95% cell viability at 40 μM, indicating both	Vyas et al.[36]

		complexes were non–toxic at effective doses. • Complexes demonstrated strong inhibition of AChE and significantly reduced Aβ aggregation.	
5.	Cobalt(III)–salnaph–pyrrolidine complex	• Cobalt(III)–based complexes were synthesized to investigate their effect on Aβ aggregation and assess their delivery across the BBB using focused ultrasound. • Octahedral Co(III) salphen and salnaph complexes showed significantly stronger inhibition than square planar Ni(II) and Pt(II) complexes due to dual binding via π–π stacking and axial coordination to histidine residues of Aβ. • ThT assay confirmed concentration-dependent inhibition of fibril formation. NMR spectroscopy and fluorescence quenching studies confirmed strong binding to N–terminal region of Aβ, particularly at His6, His13, and His14 residues. • TEM showed reduced fibril formation even at equimolar ratios. • Co(III) complexes exhibited minimal cytotoxicity in SH–SY5Y cells, making them suitable for biological studies. • Focused ultrasound successfully delivered complexes across the BBB in mice without tissue damage or behavioral changes. • Cobalt (III)–salnaph complex with pyrrolidine axial ligands showed strong inhibition of $A\beta_{1-42}$ aggregation and safe, targeted delivery.	Chan et al.[37]
6.	Dinuclear Copper(II) complexes: $Cu_2(L–RNH_2)(H_2O)_{23}$	• Three isostructural N_6O–donor ligands, derived from 2,6–bis[(bis(2–pyridylmethyl)amino)methyl]–4–methylphenol, were synthesized to chelate Cu(II), that mimic antioxidant enzymes and evaluate their potential to mitigate copper–induced oxidative stress and Aβ aggregation in AD. • The complex $Cu_2(L–RNH_2)(H_2O)_{23}$ showed the	Cendron et al.[38]

		highest copper binding affinity with log K_bind = 12.1, selective over Fe(II), Mn(II), and Zn(II), shown by potentiometric titration and UV–Vis analysis. • SOD–like activity assay yielded a low IC_{50} of 0.66 μM and a log(k_SOD) of 6.59 for complex [Cu_2(L–RNH_2)] and all complexes show SOD–like activity, while CAT–like assays confirmed rapid O_2 evolution from H_2O_2, indicating potent dual antioxidant activity. • ESI–MS confirmed selective complex formation with Cu(II) in the presence of competing metal ions, supporting its biological relevance. • The dinuclear complex Cu_2(L–RNH_2)(H_2O)$_{23}$ exhibits strong selectivity and potent antioxidant activity for mimicking natural enzymes and mitigating oxidative stress in AD.	
7.	Gadolinium(III) complex: Dyad–3 (Gd(DOTA)–cyanine dyad) (DOTA: 1,4,7,10–tetraazacyclododecane–1,4,7,10–tetraacetic acid)	• BBB–penetrable theranostic Gd(DOTA)–cyanine dyad was developed for *in vivo* and *ex vivo* imaging of Aβ in AD mouse models. • Dyad–3's interaction with Aβ was explored through fluorescence and MRI modalities in transgenic Alzheimer's mouse models. • Longitudinal relaxivity (r_1) of 4.42 $mM^{-1}s^{-1}$ was observed at 3T, and dyad–3 exhibited strong fluorescence enhancement and specific binding affinity with dissociation constants (Kd) of 90–300 μM. • Dyad–3 inhibited Aβ aggregation (IC_{50} = 2.38 μM), and significantly reduced Aβ–induced ROS generation (~30–65%) and cytotoxicity (~10–30%) in SH–SY5Y cells. • *In vivo* and *ex vivo* imaging confirmed high BBB penetrability, selective Aβ binding, and effective visualization of Aβ in transgenic Alzheimer's mice using one– and two–photon fluorescence and T1–weighted MRI.	Wang et al.[39]

		• Dyad–3 displayed good biocompatibility (LC_{50} = ~ 238 μM), rapid systemic elimination, and negligible toxicity, supporting its potential for safe diagnostic and therapeutic applications in AD.	
8.	Ruthenium(II) complex : RuApy (*cis*–$[Ru(phen)_2(3,4Apy)_2]^{2+}$)	• Water soluble metal complex *cis*–$[Ru(phen)_2(3,4Apy)_2]^{2+}$ (RuApy, 3,4Apy = 3,4–diaminopyridine, phen = 1,10–phenanthroline) effect and influence on the aggregation process and toxicity of $A\beta_{1–40}$ and its fragments during early and late stages of assembly. • RuApy was evaluated for interfering with $A\beta_{1–40}$ aggregation, and toxicity was investigated using luminescence spectroscopy, transmission electron microscopy (TEM), and *in vitro* PC12 cell assays. • TEM showed that RuApy promoted the formation of belt–like structures instead of typical fibrils, and ThT/RuApy luminescence analysis confirmed altered aggregation behavior. PC12 cells exposed to early aggregates (15 min) of $A\beta_{1–40}$ retained 100% viability in the presence of RuApy, indicating strong protective effects. • $A\beta_{1–40}$ aggregates formed in the presence of RuApy showed significantly altered morphology and reduced toxicity; full–length $A\beta_{1–40}$ was toxic at early stages but non–toxic at later stages (120 min), while RuApy neutralized early–stage toxicity even at 1:2 or 1:3 ratios. • RuApy prevented $A\beta_{1–40}$ toxicity by interacting with early oligomeric species and inducing morphological changes, possibly via electrostatic interactions, without affecting the aggregation or toxicity of $A\beta_{1–28}$, $A\beta_{11–22}$, or $A\beta_{29–40}$ fragments. • Trypan Blue exclusion assay confirmed that RuApy (upto 60 μM) was non–toxic to PC12 cells and significantly reduced $A\beta_{1–40}$ induced cytotoxicity, validating its therapeutic potential against early toxic Aβ species.	Cali et al.[40]

- RuApy complex is non–toxic to PC12 cells up to 60 μM and does not affect Aβ fragment aggregation overall, but it disrupts $A\beta_{1-40}$ aggregation and fully preserves PC12 cell viability against early–stage $A\beta_{1-40}$ toxicity.

2.2. Literature review of small molecule (chalcone–3c)

Table 2. Small molecule inhibitors of $A\beta_{42}$ aggregation.

S. No.	Small molecule	Key findings	References
1.	1–Benzylamino–2–hydroxyalkyl derivative (C18, R = 3,3–diphenylpropyl)	• Dual inhibition of $A\beta_{42}$ and tau aggregation by C18, selected from a library of 24 1–benzylamino–2–hydroxyalkyl multifunctional compounds, was investigated using *in vivo*, *in silico*, and *in vitro* kinetic studies. • C18 inhibited $A\beta_{42}$ aggregation by 80.0% and reduced preformed $A\beta_{40}$ fibrils by 63.2% at 100 μM (10:1 ratio to peptide). • Molecular docking of monomer $A\beta_{1–42}$ (PDB: 1IYT) and pentamer $A\beta_{17–42}$ (PDB: 2BEG) with C18 revealed that C18 stabilized the helical form of Aβ, interfered with oligomerization through hydrophobic and π–cation interactions, and bound centrally to misfolded tau to prevent filament elongation. • ThT fluorescence assays showed that C18 decreased the nucleation constant (k_n) 20–fold and elongation constant (k_e) 2–fold, indicating strong inhibition at early stages of $A\beta_{40}$ aggregation. • In *E. coli* cell–based assays, no toxicity was observed, validating its suitability for *in vivo* analysis.	Pasieka et al.[41]
2.	Gabapentin	• Molecular mechanism of gabapentin (GBP) inhibiting $A\beta_{1–42}$ aggregation and toxicity was investigated using *in silico* (computational docking, MD simulations) and *in vitro* neuronal assays. • Docking show favourable interactions with the $A\beta_{1–42}$ (PDB: 1IYT) peptide at both the C–terminal ($\Delta G_{binding}$ = –14.1 kcal/mol) and flexible regions ($\Delta G_{binding}$ = –25.2 kcal/mol) of monomer, with docking scores of –4.14 and –	González–Sanmiguel et al.[42]

		3.40 respectively, suggesting inhibition of several neurotoxic steps in the amyloid cascade. • Secondary structure analysis and surface roughness metrics showed reduced β–sheet content from 13.3% to 6.8%, and lowered surface roughness (from 8 ± 1 to 3 ± 0.3), indicating disrupted aggregation and increased molecular disorder in the presence of GBP. • Atomic force microscopy (AFM) showed a reduction in surface roughness from an average value of 8 ± 1 (Aβ alone) to 3 ± 0.3 (Aβ + GBP), along with a reduction in Aβ particle count from 20 ± 1 to 12 ± 0.8 per 0.25 μm^2 area. • SDS–PAGE showed that GBP reduced the presence of tetramers (to 63% of the control). • Tyrosine intrinsic fluorescence showed increased emission intensity in the presence of 250μM GBP, and confocal microscopy showed Aβ association with hippocampal neurons was reduced from 13 ± 1 to 2 ± 0.5 puncta with 100μM GBP. • GBP showed no intrinsic toxicity and reversed Aβ–induced synaptic dysfunction, restoring SV2 protein levels and postsynaptic currents without affecting baseline parameters when used alone.	
3.	Cinnamaldehyde, Phenylethyl alcohol, α–Asarone, and β–Caryophyllene	• Cinnamaldehyde (Cin), Phenylethyl alcohol (PEA), α–Asarone (ASA), and β–Caryophyllene chalcone–3c (BCP) volatile compounds were investigated for their interaction with $A\beta_{25–35}$ and $A\beta_{1–42}$ peptides using *in vitro* and *in silico* studies. • Molecular docking was conducted using $A\beta_{25–35}$ (PDB: 1XQC) and $A\beta_{1–42}$ (PDB: 1Z0Q) peptides, cin showed binding affinities of −6.609 ($A\beta_{25–35}$) and −6.557 kcal/mol ($A\beta_{1–42}$),	Dindar et al.[43]

		PEA showed −6.642 and −6.744 kcal/mol, ASA exhibited the strongest binding with −6.999 and −7.508 kcal/mol, and BCP showed −6.897 and −7.062 kcal/mol respectively, indicating all compounds interact stably with amyloid peptides. • ThT fluorescence analysis revealed that volatile compounds significantly reduced $A\beta_{25–35}$ peptide fibrillation, except for BCP at a 1:1000 ratio, which showed increased fluorescence, and 8–anilino–1–naphthalenesulfonic acid (ANS) fluorescence analysis revealed that volatile compounds, particularly PEA and BCP, reduced peptide hydrophobicity, indicating inhibited fibrillation or formation of intermediates. • Far–Ultraviolet circular dichroism (Far–UV CD) analysis showed that volatile compounds induced structural transitions in $A\beta_{25–35}$ peptide, reducing β–sheet content and increasing random coil and turn structures. – • MTT assays on SH–SY5Y neuroblastoma cells confirmed that all compounds exhibited non–significant cytotoxicity across tested molar ratios, indicating safety and potential as anti–amyloid agents. • These findings support the use of natural volatile compounds as promising candidates to inhibit amyloid fibrillation in AD.	
4.	Anthocyanidins (Cyanidin, delphinidin, malvidin, pelargonidin, peonidin, and petunidin)	• Molecular mechanism of anthocyanidins inhibiting $A\beta_{1–42}$ aggregation was investigated using *in silico* (molecular docking and MD simulations) study. • Root mean square deviation (RMSD), radius of gyration (R_g), and root mean square fluctuation (RMSF) analyses show enhanced structural stability and compactness of $A\beta_{1–42}$ (PDB: 1Z0Q), with reduced β–sheet and increased α–	Zakaria et al.[44]

		helix content. • Presence of two types of anthocyanidin, one that binds to N–terminal region (cyanidin, delphinidin, petunidin), the other that binds to SHC–C–terminal region (malvidin, pelargonidin, peonidin). • Cyanidin and malvidin were selected for MD simulations representing the N and SHC–C terminal regions due to their low binding energy, and peonidin was selected due to its different pattern of binding orientation and interactions at the SHC–C–terminal region. • The β–sheet content of $A\beta_{1-42}$ was 7% which reduced to 1% with cyanidin and malvidin and was reduced to 0% with peonidin; α–helix content increased from 38% to 42% (cyanidin), 49% (malvidin), and 53% (peonidin), indicating inhibition of aggregation and stabilization of native conformations. • Anthocyanidins inhibited β–sheet formation through two mechanisms: (i) blocking terminal interactions by binding to N– and SHC–C–terminal residues (cyanidin and malvidin) and (ii) disrupting the D23–K28 salt bridge and enhancing helicity by binding to central polar residues (peonidin).	
5.	Neferine (bisbenzylisoquinoline alkaloid derived from *Nelumbo nucifera* (lotus embryo))	• Dual regulatory effects of neferine on $A\beta_{42}$ and tau K18 aggregation were investigated using *in silico, in vitro* (ThT assay, AFM), and lab–on–a–chip technology. • RMSD and molecular docking showed that neferine binds strongly to aggregation–prone segments of $A\beta_{42}$ (PDB: 1Z0Q, 2BEG, 2NAO) and tau K18 (PDB: 5V5B, 2ON9, 5O3L). Neferine disrupted β–sheet structures and induced α–helix formation in $A\beta_{42}$ (Leu17, Val18, Phe19, Phe20) shown via MD simulations.	Nam et al.[45]

		• ThT fluorescence assay confirmed that neferine significantly decreased fibril formation and particle length for both $A\beta_{42}$ and tau K18. • Lab–on–a–chip microfluidic assays demonstrated that neferine (2.5 and 25 µM) significantly decreased ThT fluorescence intensity, confirming dissociation of pre–formed Aβ fibrils. • WST–1 assay showed that neferine reduced cytotoxicity in HT22 hippocampal cells when exposed to $A\beta_{42}$ and tau K18 fibrils. • Pharmacokinetic profiling predicted high oral absorption (HIA: 97.6%), BBB penetration (0.48), and non–inhibition of CYP enzymes (clearance rate of 1.195), suggesting drug–like properties.	
6.	ADH–353 (Cationic N–substituted oligopyrrolamide compound	• Molecular mechanism of ADH–353 disrupting $A\beta_{42}$ fibrils (PDB: 2NAO) was investigated using *in silico* (docking and MD simulations). • RMSD increased from 0.86 ± 0.04 nm to 0.98 ± 0.05 nm and RMSF from 0.33 ± 0.02 nm to 0.44 ± 0.02 nm, indicating reduced structural stability. R_g increased slightly from 1.72 ± 0.01 nm to 1.81 ± 0.09 nm, and solvent accessible surface area (SASA) increased (98.30 ± 4.92 to 100.32 ± 5.02 nm^2). • ADH–353 induced structural reorganization by decreasing β–sheet content from 28.00 ± 1.39% to 26.20 ± 0.72%, exhibiting transient helical content to 4.60 ± 0.36%, and promoting coil transitions, thereby destabilizing the aggregation–prone structure of $A\beta_{42}$. • ADH–353 disrupted interchain hydrogen bonds such as B−C from 24.04 ± 1.20 to 18.67 ± 0.93, altered hydrophobic contacts between β2–β4 regions, leading to loss of the double–horseshoe morphology of $A\beta_{42}$ fibrils.	Dabas et al.[46]

		• Molecular mechanics Poisson−Boltzmann surface area (MM–PBSA) analysis revealed strong binding ($\Delta G_{binding}$ = −142.91 ± 1.61 kcal/mol) driven by electrostatic (ΔE_{elec} = −213.32 ± 18.82 kcal/mol) and van der Waals interactions (−31.40 ± 3.33 kcal/mol). Per–residue analysis showed key contributions from Glu3, Asp7, Glu11, Glu22, Asp23, and Ala42. *In silico* absorption, distribution, metabolism, excretion, and toxicity (ADMET) predictions (log $D_{7.4}$) showed ADH–353 has good BBB permeability, high plasma protein binding, favourable lipophilicity, and a nontoxic profile, suggesting its potential as a therapeutic candidate.	
7.	Benzothiazole–piperazine hybrid molecule (Compound 1)	• Multitarget molecular mechanism of C1 was investigated against AChE (PDB: 1EVE) and $A\beta_{1–42}$ (PDB: 1IYT) using *in silico*, *in vitro*, and *in vivo* models. • MD simulations demonstrated that the benzothiazole–piperazine hybrid molecule (C1) formed stable complexes with AChE and $A\beta_{1–42}$, as indicated by stable RMSD (~0.17 ± 0.01 nm), R_g (2.28 ± 0.01 nm and 1.80 ± 0.20 nm), and SASA profiles (308 ± 0.02 nm^2 and 24.80 ± 0.20 nm^2) respectively. Molecular mechanics generalized born surface area (MM/GBSA) binding free energies were −18.64 ± 0.16 kcal/mol (AChE) and −16.10 ± 0.18 kcal/mol ($A\beta_{1–42}$), indicating favourable binding affinity. • C1 inhibited AChE with an IC_{50} of 0.42 ± 0.042 µM while showing negligible inhibition of butyrylcholinesterase (BuChE) (>100 µM). ThT assay showed reduced $A\beta_{1–42}$ aggregation by 80.70% (IC_{50} = 44.64µM) and showed 54.40% disaggregation of preformed fibrils. It also attenuated Cu^{2+}–induced Aβ aggregation. • Confocal microscopy and TEM confirmed	Mishra et al.[47]

		reduction in fibril formation; neurotoxicity assays (MTT) in SH–SY5Y and Neuro2A cells showed dose–dependent protection against H_2O_2 and okadaic acid. • *In vivo* studies in the scopolamine–induced dementia mice model revealed significant improvement in memory and learning, further supporting its potential as a CNS–active therapeutic agent.	
8.	WGalNAc (Tryptophan–Galactosylamine Conjugate)	• Molecular mechanism of WGalNAc destabilizing $A\beta_{42}$ protofibrils (PDB: 5OQV) was investigated using *in silico* study, including molecular docking and MD simulations. • Docking shows binding of WGalNAc with Val18, Phe20, and Glu22 of chain A, having a binding energy of –6.60 kcal/mol, and forming a hydrophobic contact in the CHC region. • RMSD increased from 0.33 ± 0.04 nm to 0.73 ± 0.17 nm, showing deforming the LS–shaped morphology of the fibril, R_g increased from 1.75 ± 0.02 nm to 2.01 ± 0.09 nm, and β–sheet content decreased from 57.67 to 54.67%, while coil content increased from 29.00 to 32.67%, indicating significant destabilization of the $A\beta_{42}$ protofibril in the presence of WGalNAc. • The intramolecular hydrogen bonds in the 5OQV protofibril decreased from 118.05 ± 5.90 to 116.80 ± 5.84 following the introduction of WGalNAc, indicating the destabilization of the 5OQV structure. • A greater value (89.251 ± 4.461) of the kink angle was noted upon the inclusion of WGalNAc, emphasizing WGalNAc–induced distortions within the LS–shaped 5OQV protofibril.	Dabas et al.[48]

CHAPTER 3: Computational details

3.1. Computational details of metal complex (PtRu–1)

3.1.1. Protein and ligand preparation

The structure of full–length $A\beta_{42}$ monomer (PDB: 1IYT)[49] was obtained from the research collaboratory for structural bioinformatics (RCSB) protein data bank[50] (Fig.1a). The 2D chemical structure of binuclear metal complex named PtRu–1 ($[Ru(bpy)_2(dpp)PtCl_2]Cl_2$) was drawn using ChemDraw Professional 16.0[51] (Fig. 1b). The structure was optimized by Gaussian09[52] using the DFT method employing LANL2DZ basis set.[53]

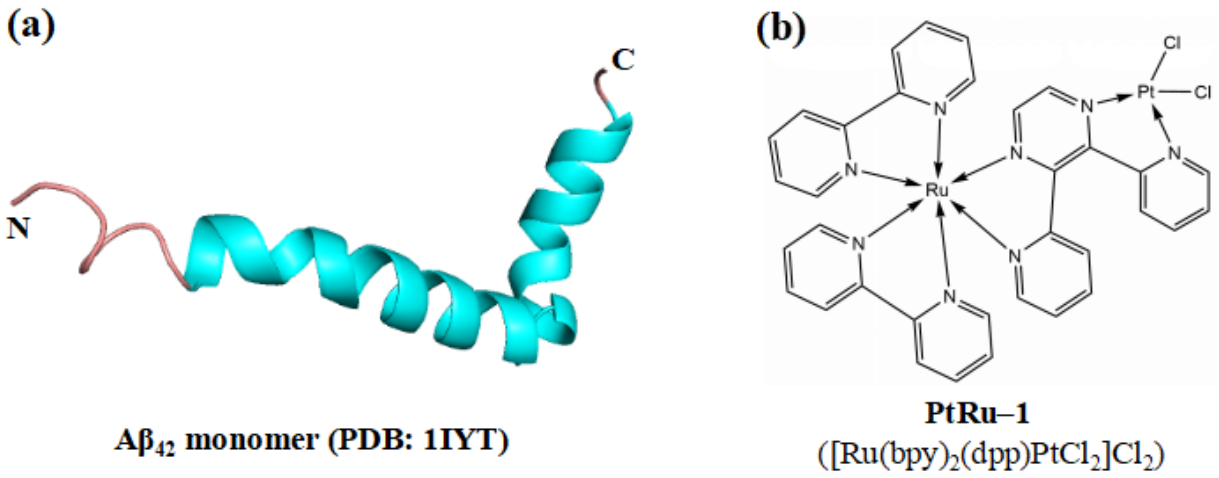

Fig. 1: Cartoon representation of $A\beta_{42}$ monomer (PDB: 1IYT) in panel a; the 2D molecular structure of PtRu–1 in panel b.

3.1.2. Molecular docking

Molecular docking was performed to calculate binding energy and key interactions of PtRu–1 with $A\beta_{42}$ monomer using AutoDock software. The PDBQT files were generated using the AutoDock Tools 1.5.7. Polar hydrogens and Kollman charges were added to the $A\beta_{42}$ monomer. The $A\beta_{42}$ monomer + PtRu–1 was enclosed within a grid box having a spacing set to 0.442 Å, and grid dimensions were set to 96 Å × 108 Å × 126 Å. The grid center was positioned at x = –0.616, y = –0.065, and z = 1.269. The Lamarckian Genetic Algorithm (LGA) was included in the docking procedure that uses the Genetic, Solis & Wets algorithm. The docking results were inspected using PyMOL[54] software.

3.2. Computational details of small molecule (chalcone–3c)

3.2.1. Protein and ligand preparation

MD simulations were conducted on two distinct systems: $A\beta_{42}$ monomer alone and $A\beta_{42}$ monomer + chalcone–3c. The amino acid sequence for $A\beta_{42}$ monomer is $D^{1}AEFRHDSGY^{10}EVHHQKLVFF^{20}AEDVGSNKGA^{30}IIGLMVGGVV^{40}IA^{42}$. The structure of full length $A\beta_{42}$ monomer (PDB: 6SZF)[55] was obtained from RCSB protein data bank[50] (Fig. 2a). The 2D chemical structure of chalcone–3c complex [(*E*)–3–(2,3–Dihydrobenzofuran–5–yl)–1–(3–fluorophenyl) prop–2–en–1–one] was drawn using ChemDraw Professional 16.0[51] (Fig. 2b). The structure was optimized by Gaussian09[52] software using DFT method and 6–31G* basis set. The Automated Topology Builder (ATB)[56] server was used to obtain AMBER99SB–ILDN force field[57] parameters for the chalcone–3c complex.

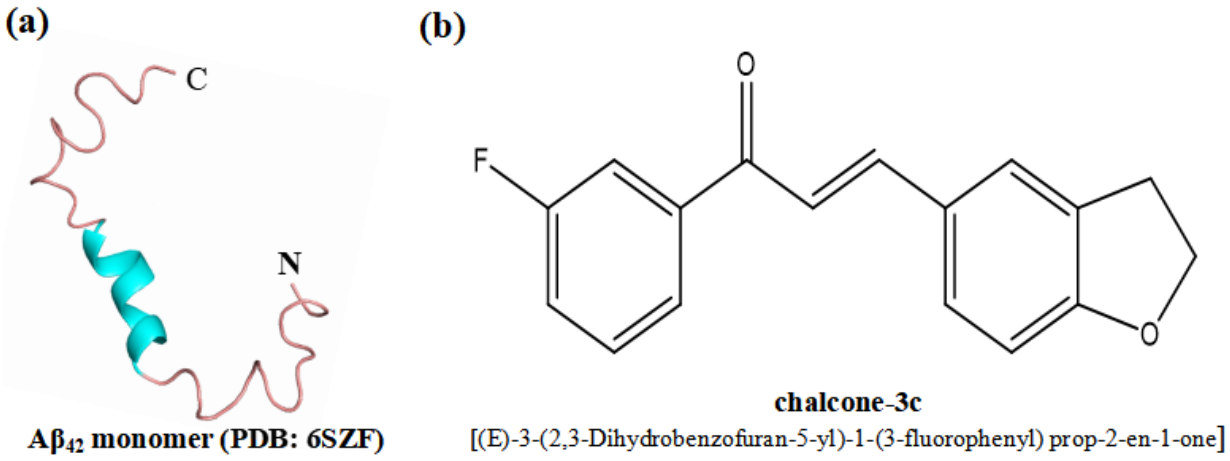

Fig. 2: Cartoon representation of $A\beta_{42}$ monomer (PDB: 6SZF) (panel a); the 2D chemical structure of chalcone−3c [(*E*)−3−(2,3−Dihydrobenzofuran−5−yl)−1−(3−fluorophenyl) prop−2−en−1−one] (panel b).

3.2.2. Molecular docking

Docking was carried out to determine the binding energy and significant interactions of chalcone–3c with $A\beta_{42}$ monomer using AutoDock Vina software.[58] The PDBQT (.pdbqt) files were generated using the AutoDock Tools 1.5.7.[59] Polar hydrogen and Kollman charges were added to the $A\beta_{42}$ monomer. The $A\beta_{42}$ monomer + chalcone–3c was enclosed within a grid box having a spacing set to 0.403 Å, and grid dimensions were set to 126 Å × 118 Å × 82 Å. The grid center was positioned at x = –11.641, y = 0.874, and z = –11.193. The LGA was included in the

docking procedure that uses the Genetic, Solis & Wets algorithm.[60] The docking results were inspected using PyMOL[54] and LigPlot+ software.[61]

3.2.3. System preparation for MD simulations

The MD simulations were performed using GROMACS 5.0.7 software[62] with AMBER99SB–ILDN force field for $A\beta_{42}$ monomer and $A\beta_{42}$ monomer + chalcone–3c complex (Table 2). The systems were positioned in a cubic box[63] having dimensions 6.51 × 6.51 × 6.51 nm^3. The systems were solvated with TIP3P water molecules[64] and the number of water molecules in $A\beta_{42}$ monomer and $A\beta_{42}$ monomer + chalcone–3c was 8751 and 8736, respectively. The concentration of NaCl (0.15 M) was incorporated in the systems to maintain neutrality of physiological pH. The steepest descent minimization algorithm was used for energy minimization, and systems were equilibrated using NVT and NPT for a period of 500 ps at 310 K temperature. For maintaining the temperature of 310 K, V–scaling method[65] was employed, and for maintaining the pressure of 1 bar Parrinello–Rahman's method[66] was used. The LINCS algorithm[67] was used to constrain bonds involving hydrogen atoms of $A\beta_{42}$ monomer, while the SETTLE algorithm was applied to constrain bonds within water. The particle mesh Ewald (PME) method[68] was used to investigate electrostatic interactions. The cut–off value for van der Waals interactions was set to 1 nm. The integration step used in MD for updating atomic positions and velocities is 2 fs. The MD trajectory was saved at an interval of every 10 ps.

Table 3. Details of MD simulated systems.

System	Simulation time (ns)	Box dimensions (nm)	Number of water molecules in box
$A\beta_{42}$ monomer	100	6.51 × 6.51 × 6.51	8751
$A\beta_{42}$ monomer + chalcone–3c	100	6.51 × 6.51 × 6.51	8736

3.2.4. Analysis details

The MD trajectories of the systems were analyzed using GROMACS 5.0.7 software. For calculating RMSD, the gmx_rms tool was used, through which backbone atoms deviation from the original position was evaluated for $A\beta_{42}$ monomer and $A\beta_{42}$ monomer + chalcone–3c. The gmx_rmsf tool[69] was used for calculating RMSF, and gmx_sasa tool[70] was used to analyze

SASA for side chain atoms of $A\beta_{42}$ monomer in contact with solvent molecules. The gmx_gyrate tool was used for analyzing the stability and compactness of the $A\beta_{42}$ monomer. The gmx_hbond tool was used for calculating intramolecular hydrogen bonds present in $A\beta_{42}$ monomer in the presence and absence of chalcone–3c. The secondary structure content was analysed using the gmx do_dssp tool.[71] Daura et al. algorithm was used for analysis of clustering by gmx_cluster.[72] The contact map was evaluated using gmx_mdmat tool. Principal component analysis (PCA) was done using gmx_covar tool to check flexibility and fluctuations in $A\beta_{42}$ monomer in the absence and presence of chalcone–3c. Free energy landscape (FEL) was performed using gmx_sham tool to get the most stable conformations.

CHAPTER 4: Results and discussion

4.1. Results and discussion of metal complex (PtRu–1)

4.1.1. Molecular docking studies and key interactions of PtRu–1 with $A\beta_{42}$ monomer

Molecular docking was performed to identify binding energy and to gain insight into the interactions of the $A\beta_{42}$ monomer residues with PtRu–1 metal complex. The PtRu–1 shows a favorable binding energy of –6.45 kcal/mol with $A\beta_{42}$ monomer. Barot et al. reported –5.4 kcal/mol binding free energy of $A\beta_{42}$ monomer with metal complex $[C_{20}H_{40}N_2O_7CoCl_2]$.[73] The nitrogen atom of bipyridine ring was involved in hydrogen bonding formation with side chain hydrogen atom (NH) of His6 and His13 residues of $A\beta_{42}$ monomer (Fig. 3a). In addition to this, $A\beta_{42}$ monomer residues (His6, His13, His14, Tyr10, and Val12) are involved in hydrophobic contacts with PtRu–1 as shown in 2D interaction map (Fig. 3b). The docking results also revealed π–π stacking interactions between the bipyridine ring of PtRu–1 and aromatic side chain of His6 and Tyr10 residues of $A\beta_{42}$ monomer. Mohammed et al. documented π–π stacking interactions between Tyr10 of $A\beta_{42}$ monomer and the indole ring of D−Trp−Aib, inhibiting the conformational transition of $A\beta_{42}$ monomer to the aggregation-prone β−sheet conformation.[74] Thus, the involvement of Tyr10 of $A\beta_{42}$ monomer in binding to PtRu–1 depicts the inhibitory potential of PtRu–1 against $A\beta_{42}$ monomer.

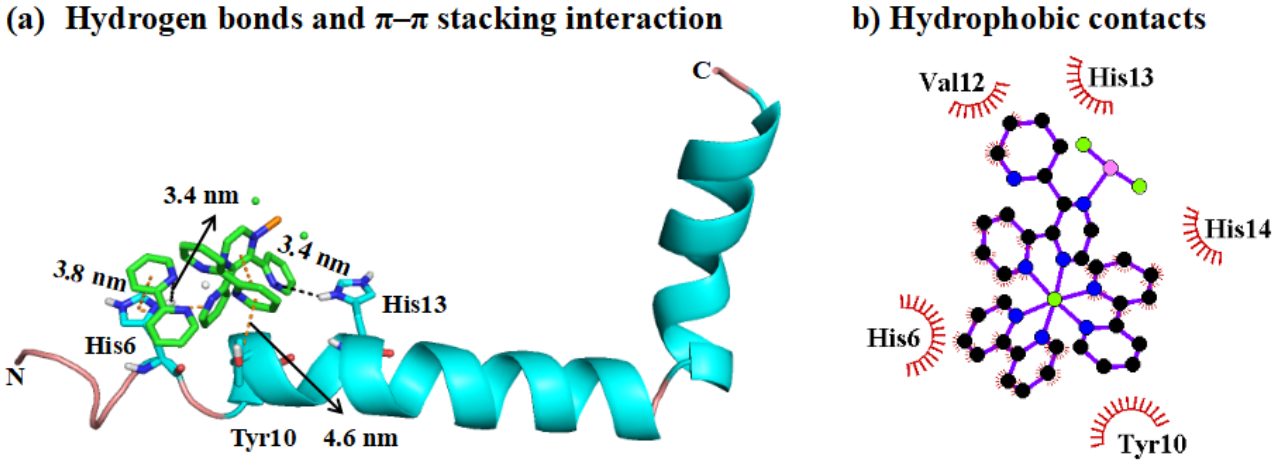

Fig. 3: Docking pose of PtRu–1 at the N–terminal region of $A\beta_{42}$ monomer, displaying hydrogen bond in dotted black line and π–π stacking in dotted orange line in panel a; 2D interaction map showing the hydrophobic contacts in red semicircles between $A\beta_{42}$ monomer residues and PtRu–1 (panel b).

Table 4. Details of key interactions of PtRu–1 with $A\beta_{42}$ monomer.

Compound	AutoDock binding energy (kcal/mol)	Residue and atoms of $A\beta_{42}$ monomer and PtRu–1 involved in hydrogen bond formation			Residues of $A\beta_{42}$ monomer involved in hydrophobic contacts with PtRu–1
		Residue	Atom[a]	Distance (nm)	
PtRu–1	–6.45	His6 His13	H:N H:N	0.34 0.34	His6, His13, His14, Tyr10, Val12

[a]Atom on the left corresponds to $A\beta_{42}$ monomer; whereas on the right corresponds to $[Ru(bpy)_2(dpp)PtCl_2]Cl_2$.

4.1.2. Parameterization for MD simulation

The parameterization of a PtRu–1 was followed using Amber MCPB.py [metal center parameter builder] and involved several stages to prepare the system and generate input files for quantum mechanical calculations and force field derivation. For the structure preparation, the PDB file of the PtRu–1 was taken from the optimized file of Gaussian. Then, the mol2 files were created for both metal Ru and Pt using the script metalpdb2mol2.py. Then, the ligand PDB file was reduced using Amber to add hydrogens to the ligand. Mol2 files were generated for non–standard residues using antechamber with appropriate net charge and GAFF atom types, following which the frcmod file was generated. PDB files were combined into a single PDB file, and pdb4amber was used to renumber atoms and residues properly. Then the mcpb.in input file was prepared in notepad, and after that ff14SB force field was used to perform the modeling that generated the pdb files for small, standard, and large models.

Then further step could not be carried out due to the abortion of the Gaussian calculation of fingerprint files highlighting the metal ion and its neighbouring environment, generated during the process.

4.2. Results and discussion of small molecule (chalcone–3c)

4.2.1. Molecular docking and key insights into interactions of chalcone–3c with Aβ42 monomer

The molecular docking of chalcone–3c with Aβ42 monomer resulted in a total of nine docked poses with binding energies ranging from –6.7 to –5.7 kcal/mol. The most favourable pose with the lowest binding energy –6.7 kcal/mol was selected (Fig. 4a). Dindar et al. reported interaction of PEA with Aβ42 monomer, having a binding energy of –6.64 kcal/mol, consistent with our study.[43] Additionally, the presence of π–π stacking was found between chalcone–3c and Phe19, Phe20 residues of Aβ42 monomer (Fig. 4a). Kirschner and coworkers reported critical role of residues Phe19 and Phe20 in CHC region of Aβ42 monomer in generation of cytotoxic oligomeric species, formed by π–π stacking interactions.[75] Similarly, Dabas et al. identified Phe19 and Phe20 residues of chain A in 50QV protofibril bind to WGalNAc, which inhibit π–π stacking interactions among phenylalanine residues in chain B, C, and D, resulting in distortion of the 50QV protofibril.[48] Thus, π–π stacking interaction between chalcone–3c and Phe19, Phe20 residues of Aβ42 monomer disrupts the possibility of π–π stacking interaction between Phe19 and Phe20 residues of Aβ42 monomer, inhibiting Aβ42 aggregation. The residues (Glu22, Val18, Phe19, and Phe20) of Aβ42 monomer displayed hydrophobic contacts with chalcone–3c (Fig. 4b).

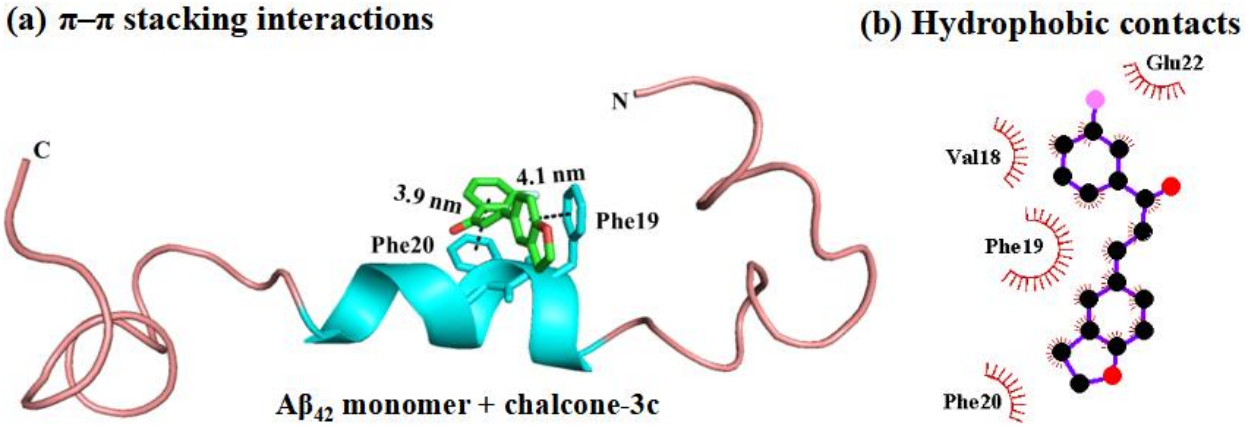

Fig. 4: The most favourable docked pose of Aβ42 monomer + chalcone–3c, displaying π–π stacking interactions in dotted black line (panel a); the 2D interaction map displaying hydrophobic contacts in red semicircles between Aβ42 monomer and chalcone–3c (panel b).

The dominant contribution of the CHC region (Val18, Phe19, Phe20, and Glu22) in binding to chalcone–3c highlights its inhibition potential against $A\beta_{42}$ monomer. The MD simulations were performed to gain insights into the inhibitory actions of chalcone–3c against $A\beta_{42}$ monomer.

4.2.2. Impact of chalcone–3c on conformational fluctuations in $A\beta_{42}$ monomer

RMSD and RMSF analyses were conducted to assess the convergence of MD simulation and structural stability of $A\beta_{42}$ monomer in the presence and absence of chalcone–3c. The average RMSD of $A\beta_{42}$ monomer was noted to be 1.24 ± 0.06 nm (Fig. 5a). Upon the incorporation of the chalcone–3c, the average RMSD of the $A\beta_{42}$ monomer decreased to 1.01 ± 0.05 nm (Fig. 5a), indicating reduced fluctuations of the $A\beta_{42}$ monomer. The RMSD value of the $A\beta_{42}$ monomer decreases by 0.23 nm in the presence of the chalcone–3c. These findings align well with the results reported by Kaur et al., showing a decrease in RMSD value from 1.14 to 1.0 nm after interaction of tacrine–benzofuran hybrid C1 with $A\beta_{42}$ monomer.[76]

The RMSF analysis indicates an average value of 0.72 ± 0.04 nm for the $A\beta_{42}$ monomer, which reduced to 0.56 ± 0.03 nm in the presence of the chalcone–3c (Fig. 5b). The RMSF analysis indicated that the fluctuations reduced drastically and specifically in the residual region Asp1–His6, Val12–Gln15, Phe19, Ala21, Glu22, Ser26–Ala30, Gly33, Val36–Val39, depicting lower conformational flexibility of the $A\beta_{42}$ residues in presence of the chalcone–3c. The reduced conformational flexibility of $A\beta_{42}$ monomer in the presence of chalcone–3c highlights the reduced aggregation propensity of $A\beta_{42}$.

4.2.3. SASA and R_g evaluation of $A\beta_{42}$ monomer before and after incorporation of chalcone–3c

SASA analysis was carried out to check $A\beta_{42}$ monomer exposure to solvent molecules in the presence and absence of chalcone–3c. The SASA of $A\beta_{42}$ monomer diminished from 42.42 ± 2.12 to 39.74 ± 1.98 nm upon the inclusion of chalcone–3c (Fig. 5c). The lower SASA value indicates reduced exposure of $A\beta_{42}$ monomer to solvent in the presence of chalcone–3c, suggesting a decreased propensity for self–aggregation of $A\beta_{42}$ monomer.

R_g was evaluated to analyze the compactness of protein and to check the stability of protein in the presence and absence of chalcone–3c. The average R_g value of $A\beta_{42}$ monomer in presence of chalcone–3c was reduced to 0.88 ± 0.04 from 1.06 ± 0.05 nm (Fig. 5d), which is in correlation with the results published by Zakaria et al., showing decrease in R_g value from 1.03 to 0.94 nm

upon binding of malvidin with Aβ$_{42}$ monomer.[44] The decrease in R_g value signifies reduced compactness of Aβ$_{42}$ monomer when simulated with chalcone–3c, thereby reducing its tendency to self–aggregate.

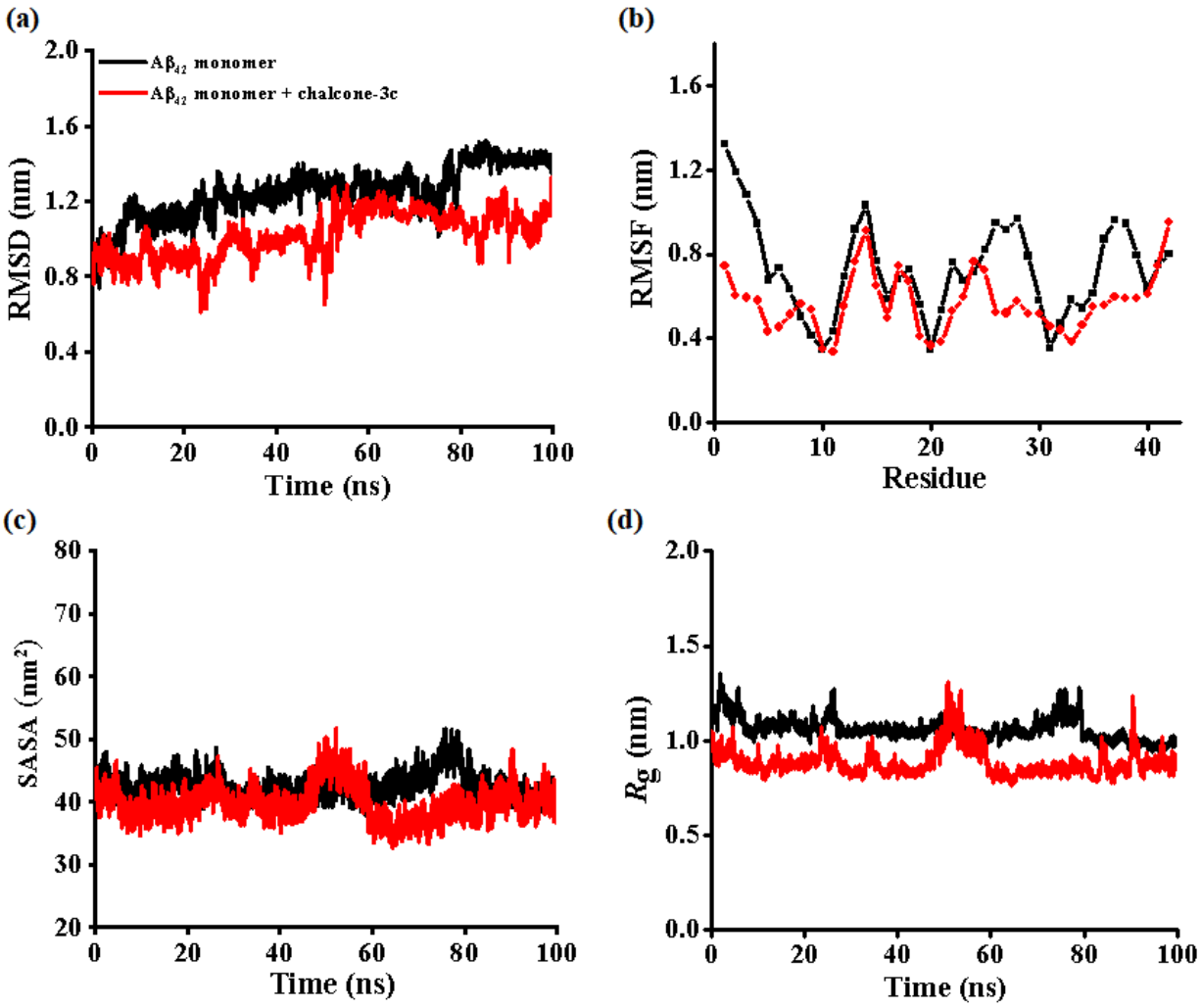

Fig. 5: RMSD for the backbone atoms (panel a); RMSF calculated for Cα atoms (panel b); SASA for side chain atoms (panel c); R_g calculated for compactness (panel d) for Aβ$_{42}$ monomer before and after incorporation of chalcone–3c.

4.2.4. Effect of chalcone–3c on intramolecular hydrogen bonding in Aβ$_{42}$ monomer

The intramolecular hydrogen bonding is a non–covalent interaction that accounts for the stability of Aβ$_{42}$ monomer in the presence and absence of chalcone–3c. The average number of intramolecular hydrogen bonds increased from 21.37 ± 0.04 to 22.19 ± 0.04 upon interaction of chalcone–3c with Aβ$_{42}$ monomer (Fig. 6). Zakaria et al. reported an increase in intramolecular

hydrogen bonds from 25.74 to 26.41 after effective binding of peonidin with Aβ$_{42}$ monomer.[44] The increase in intramolecular hydrogen bonds accounts for stabilization of Aβ$_{42}$ monomer.

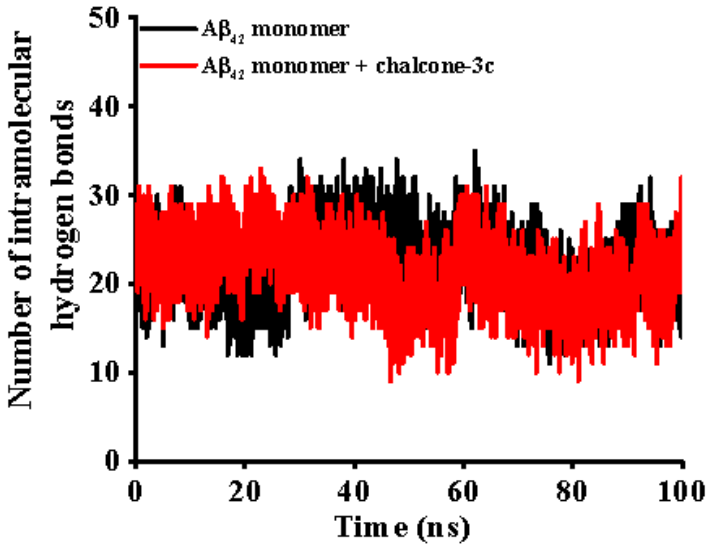

Fig. 6: Intramolecular hydrogen bonds in Aβ$_{42}$ monomer and Aβ$_{42}$ monomer + chalcone–3c.

4.2.5. Variation in the secondary structural preferences of Aβ$_{42}$ monomer with the inclusion of chalcone–3c

The variation in secondary structure of Aβ$_{42}$ monomer upon inclusion of chalcone–3c was analyzed using secondary structure analysis. The Aβ$_{42}$ monomer achieved 20.2 ± 1.6% helix, 1.4 ± 1.2% β–sheet, 18.4 ± 3.2% bend, 33.4 ± 4.5% coil, and 23.6 ± 2.3% turn (Table 5). The Aβ$_{42}$ monomer in the presence of chalcone–3c achieved 33.8 ± 1.5% helix, 1.2 ± 1.0% β–sheet, 9.0 ± 2.2% bend, 32.8 ± 2.8% coil, and 26.4 ± 3.2% turn (Table 5). The inclusion of chalcone–3c shows major variation in increased helix content, followed by a decrease in bend content, which confirms the inhibition of Aβ$_{42}$ monomer aggregation. Kaur et al. revealed an increase in helical content of Aβ$_{42}$ monomer to 33.0 ± 2.9% in the presence of mono triazole derivative (4v), which is correlated with our findings, that inhibit the conformational transition from helical to β–sheet structure and hence prevent Aβ$_{42}$ monomer aggregation.[77]

Table 5. Modulation in secondary structure content of monomer in absence and presence of chalcone–3c.

Secondary structure content (%)	$A\beta_{42}$ monomer	$A\beta_{42}$ monomer + chalcone–3c
Helix[a]	20.2 ± 1.6	33.8 ± 1.5
β–sheet[b]	1.4 ± 1.2	1.2 ± 1.0
Coil	33.4 ± 4.5	32.8 ± 2.8
Bend	18.4 ± 3.2	9.0 ± 2.2
Turn	23.6 ± 2.3	26.4 ± 3.2

[a]Helix = α–helix + π–helix + 3_{10}–helix; [b]β–sheet = β–strand + β–bridge

The per–residue secondary structure analysis was performed to find out the contribution of each amino acid residue to the overall secondary structure. The presence of chalcone–3c has led to increased helical content in the region of Ala2, Glu3, Phe4, His14, Gln15, and Ser26–Ile31 (SNKGAI) (Fig. 7a). A remarkable increase in helical content in the CHC region Lys16–Ala21 has led to a reduction in self–aggregation tendency of $A\beta_{42}$ monomer. This was followed by decrease in coil content in the region Asp1–Glu4, Asp23–Gly25, Gly29 and Gly33 that account for their conversion to helical conformation (Fig. 7b). There was a notable reduction in bend for residues Phe4, Arg5, Lys16–Ser26 and Ala30–Gly33 of $A\beta_{42}$ monomer (Fig. 7c). The turn content reduced for residues Phe4, Arg5, Asp7–His13, Ala21–Asp23, Ser26, Asn27, Ile31–Gly33 of $A\beta_{42}$ monomer (Fig. 7d). Therefore, the presence of chalcone–3c preserved the native helical content by blocking the conformation transition to coil, bend and turn structure, suggesting the inhibitory role of chalcone–3c against self–aggregation of $A\beta_{42}$ monomer and inhibiting its aggregation.

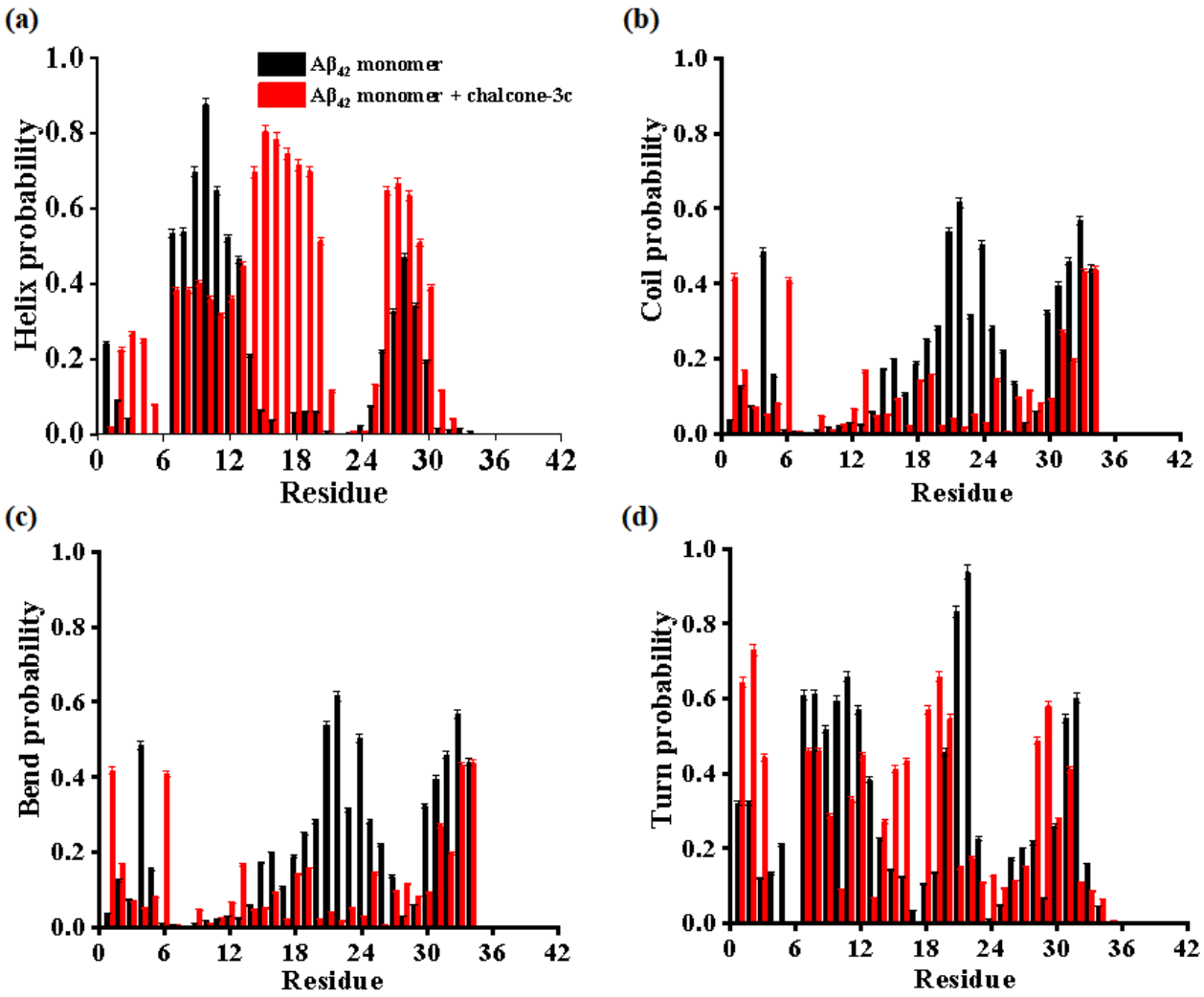

Fig. 7: Residue-wise secondary structure analysis showing probability of helix (panel a), coil (panel b), bend (panel c), and turn (panel d).

4.2.6. Effect on conformational homogeneity of Aβ42 monomer in presence and absence of chalcone–3c

The thermodynamic stability of Aβ42 monomer was evaluated using conformational clustering, both in the absence and presence of chalcone–3c. The conformations observed in the most populated microstates were recorded as 4.9%, 4.67% and 3.69% (C_1, C_2, C_3) in Aβ42 monomer (Fig. 8a). Similarly, conformations observed in the most populated microstates for Aβ42 monomer + chalcone–3c were found to be 23.78%, 16.66% and 13.42% (C_1, C_2, C_3). This increase in conformations in the most populated microstate C_1 (from 4.9 to 23.78%) illustrates conformational homogeneity within the MD ensemble of Aβ42 monomer + chalcone–3c.

Additionally, sampling in the top three microstates in Aβ$_{42}$ monomer + chalcone–3c was observed to be higher at 53.88% compared to 13.36% in Aβ$_{42}$ monomer. The key interactions of chalcone–3c with Aβ$_{42}$ monomer in the representative conformation of C_1 were examined. The oxygen atom of furan ring of chalcone–3c was involved in hydrogen bonding with the main chain hydrogen atom of NH of Asn27 residue of Aβ$_{42}$ monomer in the representative conformation (Fig. 8b). The Aβ$_{42}$ monomer residues Gly9, Tyr10, Glu11, Val24, Ile32 and Met35 were involved in formation of hydrophobic contacts with chalcone–3c (Fig. 8c). The conformational clustering analysis revealed a consistent conformational ensemble of Aβ$_{42}$ monomer in the presence of chalcone–3c that inhibit the aggregation tendency of Aβ$_{42}$ monomer.

Table 6. Influence of chalcone–3c on conformational homogeneity of Aβ$_{42}$ monomer.

System	Microstates		
	C_1	C_2	C_3
Aβ$_{42}$ monomer	4.9	4.67	3.69
Aβ$_{42}$ monomer + chalcone–3c	23.78	16.66	13.42

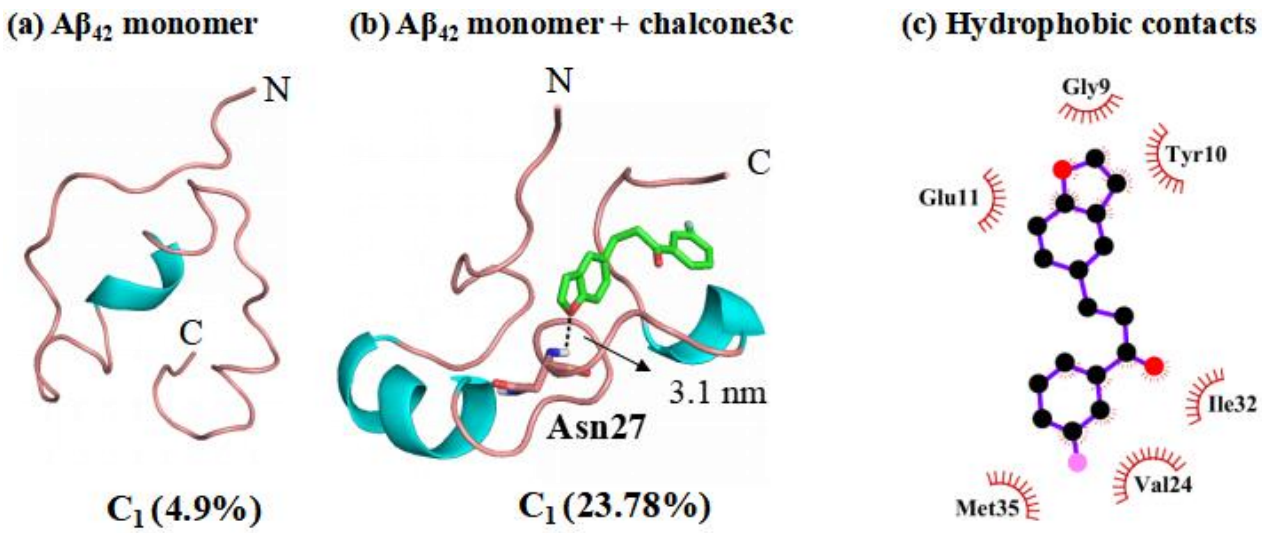

Fig. 8: Highest populated conformation state (C_1) of Aβ$_{42}$ monomer (panel a); hydrogen bonding between chalcone–3c and Aβ$_{42}$ monomer (panel b); 2D interaction map displaying hydrophobic contacts between chalcone–3c and Aβ$_{42}$ monomer in C_1 (panel c).

4.2.7. Binding of chalcone–3c modifies intrapeptide contact patterns in $A\beta_{42}$ monomer

To elucidate the side chain–side chain interactions within the $A\beta_{42}$ monomer, the contact maps were generated that emphasize the changes in the intrapeptide interactions of $A\beta_{42}$ monomer before and after inclusion of chalcone–3c. The interactions between the $A\beta_{42}$ monomer residues Lys16–Ala21 and Ala30–Ile41 were disturbed upon the incorporation of chalcone–3c (Fig. 9). The disruption of intramolecular side chain–side chain interactions has led to a decreased propensity for $A\beta_{42}$ monomer self–aggregation. Singh et al. reported a reduction in the contacts between Asp1–Val12 and Ser26–Ile41 residues of $A\beta_{42}$ monomer in the presence of a decapeptide, D–enantiomeric RTHLVFFARK–NH_2 (rk10), indicating $A\beta_{42}$ monomer stabilization, which is in correlation with the present study.[78]

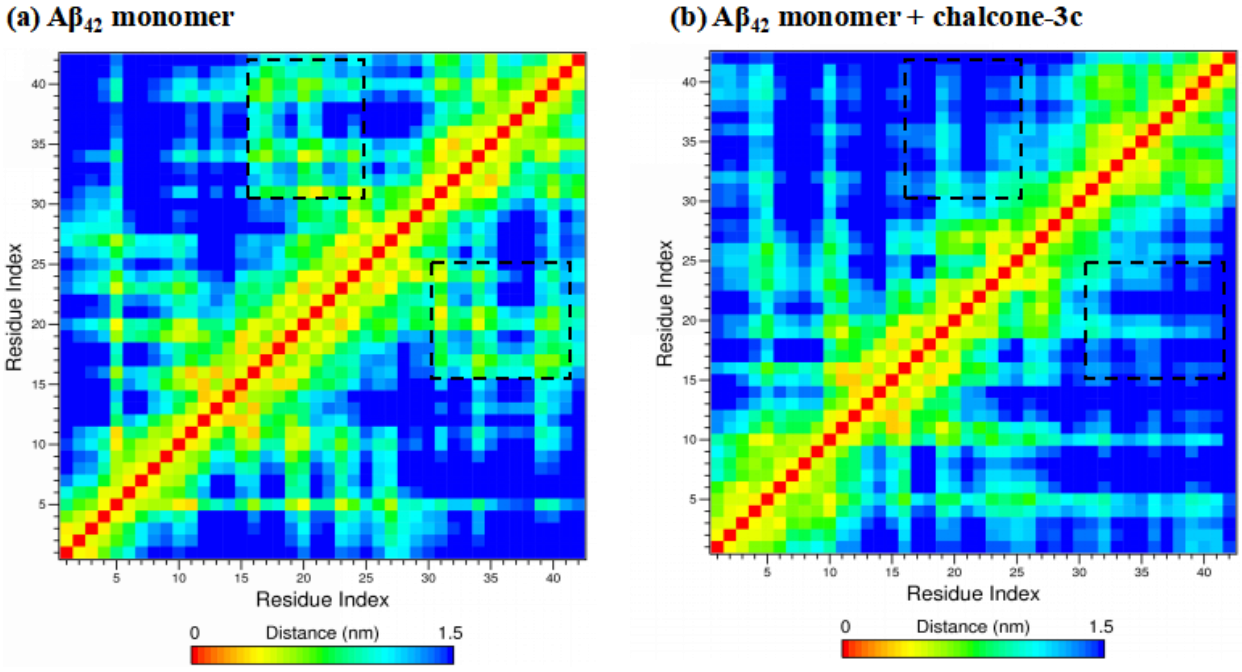

Fig. 9: Contact map side chain–side chain interactions within the $A\beta_{42}$ monomer (panel a) and in presence of chalcone–3c (panel b).

4.2.8. PCA and FEL of $A\beta_{42}$ monomer and $A\beta_{42}$ monomer + chalcone–3c

PCA assesses protein mobility by extracting conformations characterized by eigenvalues and eigenvectors, which determine the atomic motions of the complex. The flexibility in confirmation was analyzed from the trace value of Cα atoms of the covariance matrix. The trace value obtained was 24.40 nm^2 for $A\beta_{42}$ monomer, which reduced significantly to 14.35 nm^2 for

$A\beta_{42}$ monomer + chalcone–3c (Fig. 10). This decrease in trace value signifies a reduction in conformational dynamics that is correlated with RMSF analysis (Fig. 5b).

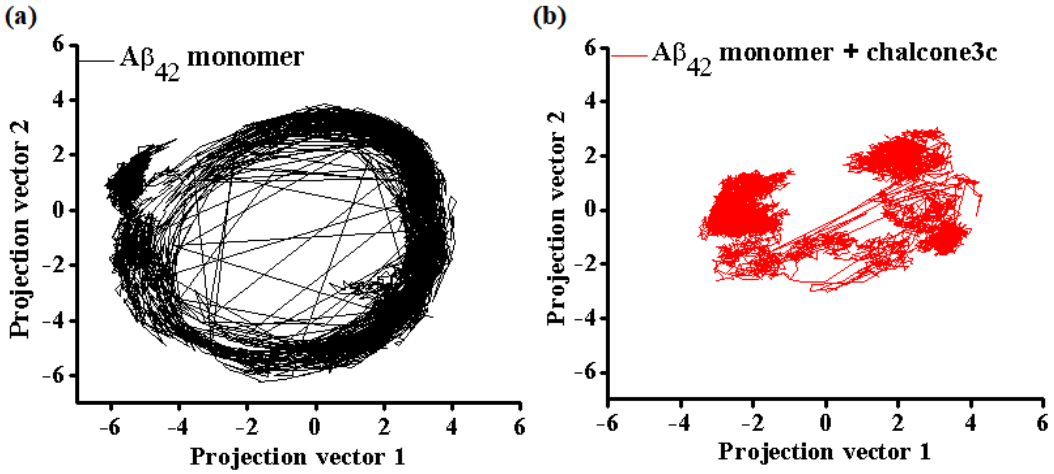

Fig. 10: 2D projection of simulated trajectories with eigenvectors 1 and 2 for $A\beta_{42}$ monomer and $A\beta_{42}$ monomer + chalcone–3c.

FEL was produced to analyze conformational variation using PC1 and PC2 components. The FEL of $A\beta_{42}$ monomer exhibits a unique minimum–energy basin and many metastable states linked by energy barriers. The FEL indicates that the energy ranges from 0 to 3.71 kcal/mol for $A\beta_{42}$ monomer and 0 to 0.83 kcal/mol for $A\beta_{42}$ monomer + chalcone–3c (Fig. 11), emphasizing the distinct conformational subspaces in the two systems. The reduction in area of free energy landscape in terms of decrease in scale (by 4.46 units) in $A\beta_{42}$ monomer + chalcone–3c signifies reduced conformational space (Fig. 11). The reduction in conformational subspace enhances conformational stability and limits dynamic flexibility that leads to a reduction in self aggregation propensity of $A\beta_{42}$ monomer. Additionally, minimum energy conformations were extracted and evaluated for their secondary structure propensity (Table 7). The minimum energy conformations extracted for $A\beta_{42}$ monomer exhibit 7% helix, 24% bend, 33% coil, 10% β–sheet, and 24% turn. The data indicated loss of native helical conformation of $A\beta_{42}$ monomer and transition into predominant coil conformation, in accordance with secondary structure results (Table 5). However, FEL of $A\beta_{42}$ monomer + chalcone–3c depicts two minimum energy basins (i'–ii') that exhibited 17–10% helix, 40% turn, 10–17% bend, and 33% coil. The presence of chalcone–3c diminished β–sheet content completely in the minimum energy conformation, displaying its inhibitory effect on $A\beta_{42}$ monomer aggregation. Remarkably high helical content

was observed after inclusion of chalcone–3c that enhances the conformational stability of Aβ$_{42}$ monomer.

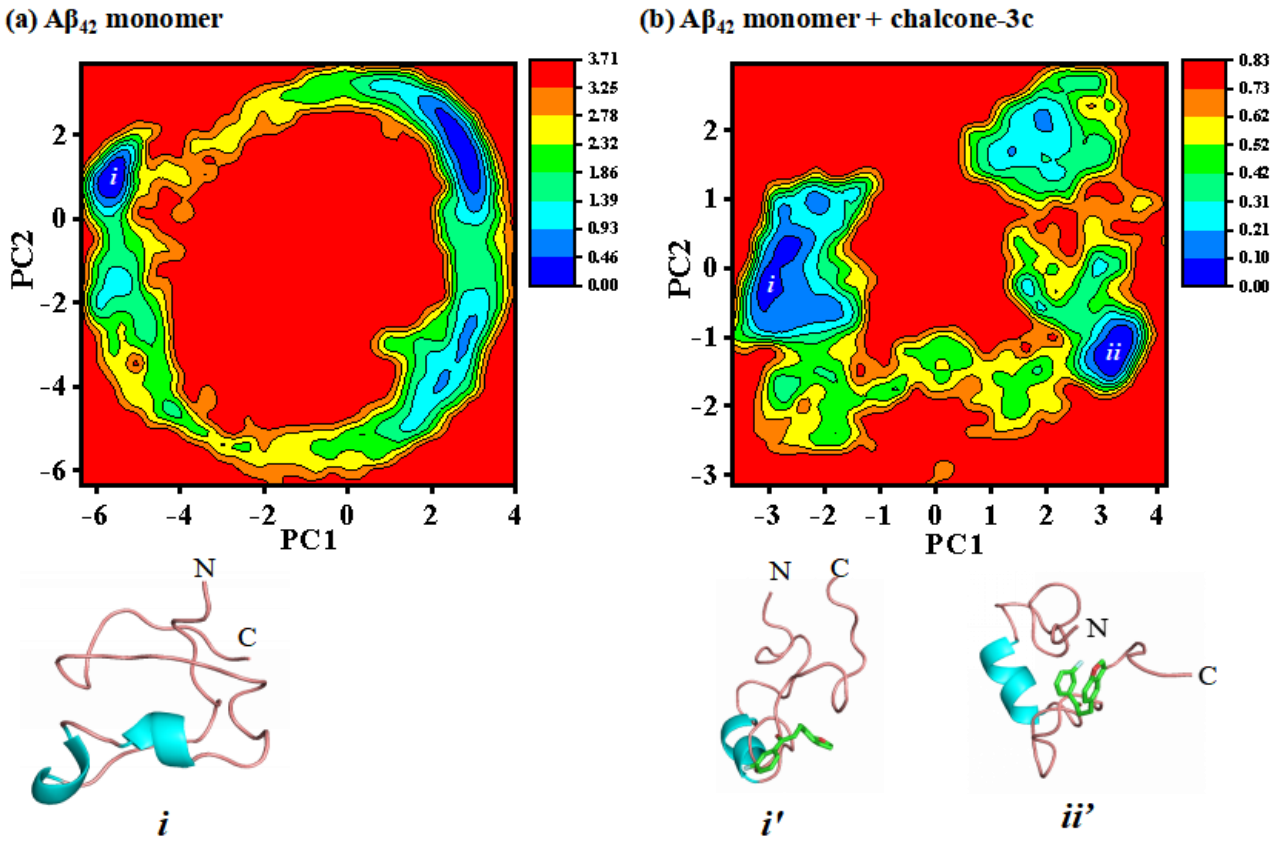

Fig. 11: FEL for Aβ$_{42}$ monomer (panel a) and Aβ$_{42}$ monomer + chalcone–3c (panel b) showing minimum energy conformations.

Table 7. Secondary structure content of FEL conformations.

System	Conformation	Secondary structure component (%)				
		Helix[a]	β–sheet[b]	Coil	Bend	Turn
Aβ$_{42}$ monomer	*i*	7	10	36	24	24
Aβ$_{42}$ monomer +	*i'*	17	0	33	10	40
Chalcone–3c	*ii'*	10	0	33	17	40

[a]Helix = α–helix + π–helix + 3$_{10}$–helix; [b]β–sheet = β–strand + β–bridge

CHAPTER 5: Conclusions

The study on binuclear metal complex PtRu–1 employed molecular docking to assess the binding affinity and interaction profile of the PtRu–1 with $A\beta_{42}$ monomer (PDB: 1IYT). The PtRu–1 exhibited binding energy of −6.45 kcal/mol with $A\beta_{42}$ monomer and showed favorable π–π stacking interactions with His6 and Tyr10, and hydrogen bonds with His6 and His13 of $A\beta_{42}$ monomer. PtRu–1 displayed hydrophobic contacts with residues (His6, His13, His14, Tyr10, and Val12) that altogether account for the inhibitory potential of PtRu–1 against self–aggregation propensity of $A\beta_{42}$ monomer. However, MD simulations could not be performed due to technical constraints, hence limiting further understanding of the dynamic behavior and structural stability of the complex within the binding site.

The study on small molecule (chalcone–3c), utilized molecular docking, and MD simulations to understand the inhibitory effect of chalcone–3c on $A\beta_{42}$ monomer (PDB: 6SZF) self–aggregation. RMSD, RMSF, SASA, and R_g analyses demonstrated that chalcone–3c reduces structural fluctuations in the $A\beta_{42}$ monomer, hence reducing the aggregation. A significant increase in the helical content in $A\beta_{42}$ monomer from 20.2 ± 1.6% to 33.8 ± 1.5% was noted in the presence of chalcone–3c, thereby stabilizing $A\beta_{42}$ monomer by inhibiting conformational changes towards aggregation−prone structures. Chalcone–3c exhibits π–π stacking interactions with the CHC region residues Phe19 and Phe20, and hydrophobic contacts with Glu22, Val18, Phe19, and Phe20 that blocks the self-fibrillation $A\beta_{42}$ monomer. PCA and FEL analysis revealed enhanced conformational homogeneity of $A\beta_{42}$ monomer in the presence of chalcone–3c, characterized by enhanced helical content and disappearance of aggregation−prone β–sheet structures. Hence, illumination of the inhibition mechanism of chalcone–3c against $A\beta_{42}$ monomer self–aggregation, provides significant insights, which will guide the strategic design of potent new small−molecule inhibitors to prevent $A\beta_{42}$ aggregation in AD.

References

1. Du, X.; Li, Y.; Xia, Y.L.; Ai, S.M.; Liang, J.; Sang, P.; Ji, X.L.; Liu, S.Q. Insights into protein–ligand interactions: mechanisms, models, and methods. *Int. J. Mol. Sci.* **2016**, *17*, 144.
2. Soto, C. Unfolding the role of protein misfolding in neurodegenerative diseases. *Nat. Rev. Neurosci.* **2003**, *4*, 49−60.
3. Better, M.A. Alzheimer's disease facts and figures. *Alzheimers Dement*. **2023**, *19* 1598−1695.
4. Cummings, J. New approaches to symptomatic treatments for Alzheimer's disease. *Mol. Neurodegener.* **2021**, *16*, 1−13.
5. Murphy, M.P.; Buzinova, V.A.; Johnson, C.E. The amyloid−β peptide: Guilty as charged?. *Biochem. Biophys. Acta. Mol. Basis. Dis.* **2024**, *1870*, 166945.
6. Abelein, A. Metal binding of Alzheimer's amyloid−β and its effect on peptide self−assembly. *ACC Chem. Res.* **2023**, *56*, 2653−2663.
7. Yu, N.; Pasha, M.; Chua, J.J.E. Redox changes and cellular senescence in Alzheimer's disease. *Redox Biol.* **2024**, *70, 103048*.
8. Singh, K.; Kaur, A.; Goyal, B.; Goyal, D. Harnessing the therapeutic potential of peptides for synergistic treatment of Alzheimer's disease by targeting Aβ aggregation, metal−mediated Aβ aggregation, cholinesterase, tau degradation, and oxidative stress. *ACS Chem. Neurosci.* **2024**, *15*, 2545−2564.
9. Zaman, M.; Khan, A.N.; Zakariya, S.M.; Khan, R.H. Protein misfolding, aggregation and mechanism of amyloid cytotoxicity: An overview and therapeutic strategies to inhibit aggregation. *Int. J. Biol. Macromol*. **2019**, *134*, 1022–1037.
10. Qiu, T.; Liu, Q.; Chen, Y.X.; Zhao, Y.F.; Li, Y.M. $A\beta_{42}$ and $A\beta_{40}$: Similarities and differences. *J. Pept. Sci.* **2015**, *21*, 522−529.
11. Tiwari, M.K.; Kepp, K.P. Modeling the aggregation propensity and toxicity of amyloid−β variants. *J. Alzheimers Dis.* **2015**, *47*, 215−229.
12. Savelieff, M.G.; Lee, S.; Liu, Y.; Lim, M.H. Untangling amyloid−β, tau, and metals in Alzheimer's disease. *ACS Chem. Biol.* **2013**, *8*, 856−865.
13. Puentes−Díaz, N.; Chaparro, D.; Morales−Morales, D.; Flores−Gaspar, A.; Alí−Torres, J. Role of metal cations of copper, iron, and aluminum and multifunctional ligands in Alzheimer's disease: Experimental and computational insights. *ACS omega* **2023**, *8*, 4508−4526.
14. Zhao, Y.J.; Xu, K.F.; Shu, F.X.; Zhang, F. Neurotropic virus infection and neurodegenerative diseases: Potential roles of autophagy pathway. *CNS Neurosci. Ther.* **2024**, *30*, 14548.
15. Pathak, C.; Kabra, U.D. A comprehensive review of multi−target directed ligands in the treatment of Alzheimer's disease. *Bioorg. Chem.* **2024** *144*, 107152.

16. Peng, Y.; Jin, H.; Xue, Y.H.; Chen, Q.; Yao, S.Y.; Du, M.Q.; Liu, S. Current and future therapeutic strategies for Alzheimer's disease: An overview of drug development bottlenecks. *Front. Aging Neurosci*, **2023**, *15*, 1206572.

17. (a) Cuajungco, M.P.; Frederickson, C.J.; Bush, A.I. Amyloid–β metal interaction and metal chelation. *Subcell. Biochem.* **2005**, 235–254. (b) Tahmasebinia, F.; Emadi, S. Effect of metal chelators on the aggregation of beta–amyloid peptides in the presence of copper and iron. *Biometals* **2017**, *30*, 285–293. (c) Rulmont, C.; Stigliani, J.L.; Hureau, C.; Esmieu, C. Rationally designed Cu (I) ligand to prevent CuAβ−generated ROS production in the Alzheimer's disease context. *Inorg. Chem.* **2024**, *63*, 2340−2351. (d) Gucký, A.; Hamuľaková, S. Targeting biometals in Alzheimer's disease with metal chelating agents including coumarin derivatives. *CNS Drugs.* **2024**, *38*, 507–532.

18. (a) Jokar, S.; Khazaei, S.; Gameshgoli, X.E.; Khafaji, M.; Yarani, B.; Sharifzadeh, M.; Beiki, D.; Bavi, O. Amyloid β–targeted inhibitory peptides for Alzheimer's disease: Current state and future perspectives. *Exon Publications* **2020**, 51–68. (b) Sehra, N.; Parmar, R.; Maurya, I.K.; Kumar, V.; Tikoo, K.; Jain, R. Synthesis and mechanistic study of ultrashort peptides that inhibits Alzheimer's Aβ−aggregation−induced neurotoxicity. *Bioorg. Chem.* **2024**, *144*, 107159.

19. Marasco, D.; Vicidomini, C.; Krupa, P.; Cioffi, F.; Huy, P.D.Q.; Li, M.S.; Florio, D.; Broersen, K.; De Pandis, M.F.; Roviello, G.N. Plant isoquinoline alkaloids as potential neurodrugs: A comparative study of the effects of benzo [c] phenanthridine and berberine–based compounds on β–amyloid aggregation. *Chem. Biol. Interact.* **2021**, *334*, 109300.

20. Yoo, K.Y.; Park, S.Y. Terpenoids as potential anti–Alzheimer's disease therapeutics. *Molecules* **2012**, *17*, 3524–3538.

21. Guzzi, C.; Colombo, L.; Luigi, A.D.; Salmona, M.; Nicotra, F.; Airoldi, C. Flavonoids and their glycosides as anti-amyloidogenic compounds: $A\beta_{1-42}$ interaction studies to gain new insights into their potential for Alzheimer's disease prevention and therapy. *Chem. Asian J.* ***2017***, *12*, 67–75.

22. Khan, H.Y.; Ahmad, A.; Hassan, M.N.; Khan, Y.H.; Arjmand, F.; Khan, R.H. Advances of metallodrug−amyloid β aggregation inhibitors for therapeutic intervention in neurodegenerative diseases: Evaluation of their mechanistic insights and neurotoxicity. *Coord. Chem. Rev.* **2024**, *501*, 215580.

23. (a) Mishra, C.B.; Shalini, S.; Gusain, S.; Kumar, P.; Kumari, S.; Choi, Y.S.; Kumari, J.; Moku, B.K.; Yadav, A.K.; Prakash, A.; Jeon, R. Multitarget action of benzothiazolepiperazine small hybrid molecule against Alzheimer's disease: *In silico*, *in vitro*, and *in vivo* investigation. *Biomed. Pharmacother.* **2024**, *174*, 116484. (b) Nam, Y.; Prajapati, R.; Kim, S.; Shin, S.J.; Park, Y.H.; Park, H.H.; Lim, D.; Yoon, Y.; Lee, G.; Jung, H.A.; Park, I. Dual regulatory effects of neferine on amyloid−β and tau aggregation studied by *in silico*, *in vitro*, and lab−on−a−chip technology. *Biomed. Pharmacother.* **2024**, *172*, 116226 (c) Hadidi, S.; Farzaei, M.H. Inhibitory activity of natural flavonoids against protein aggregation in Alzheimer's disease: A computational simulation study. *Adv. J. Chem. Sect. A.* **2023**, *6*, 123−140. (d) Chen, X.; Li, Y.; Kang, J.; Ye, T.; Yang, Z.; Liu, Z.; Liu, Q.; Zhao, Y.; Liu, G.; Pan, J. Application of a novel coumarin derivative near−infrared fluorescence

probe to amyloid−β imaging and inhibition in Alzheimer's disease. *J. Lumin.* **2023**, *256*, 119661. (e) Wang, X.X.; Xie, F.; Jia, C.C.; Yan, N.; Zeng, Y.L.; Wu, J.D.; Liu, Z.P. Synthesis and biological evaluation of selective histone deacetylase 6 inhibitors as multifunctional agents against Alzheimer's disease. *Eur. J. Med. Chem.* **2021**, *225*, 113821.

24. Suh, J.M.; Kim, G.; Kang, J.; Lim, M.H. Strategies employing transition metal complexes to modulate amyloid−β aggregation. *Inorg. Chem.* **2018,** *58*, 8−17.
25. He, L.; Wang, X.; Zhu, D.; Zhao, C.; Du, W. Methionine oxidation of amyloid peptides by peroxovanadium complexes: Inhibition of fibril formation through a distinct mechanism. *Metallomics* **2015**, *7*, 1562−1572.
26. Ma, G.; Huang, F.; Pu, X.; Jia, L.; Jiang, T.; Li, L.; Liu, Y. Identification of [PtCl2 (phen)] binding modes in amyloid-β peptide and the mechanism of aggregation inhibition. *Chem. Eur. J.* **2011**, *17*, 11657–11666.
27. Cohen, S. M.; Lippard, S. J. Cisplatin: From DNA damage to cancer chemotherapy. *Prog. Nucleic Acid Res. Mol. Biol.* **2001**, *67*, 93–130.
28. Kumar, A.; Moody, L.; Olaivar, J.F.; Lewis, N.A.; Khade, R.L.; Holder, A.A.; Zhang, Y.; Rangachari, V. Inhibition of $A\beta_{42}$ peptide aggregation by a binuclear ruthenium (II)−platinum (II) complex: Potential for multimetal organometallics as anti-amyloid agents. *ACS Chem. Neurosci.* **2010**, *1*, 691-701.
29. Barnham, K.J.; Kenche, V.B.; Ciccotosto, G.D.; Smith, D.P.; Tew, D.J.; Liu, X.; Perez, K.; Cranston, G.A.; Johanssen, T.J.; Volitakis, I.; Bush, A.I. Platinum−based inhibitors of amyloid−β as therapeutic agents for Alzheimer's disease. *Proc. Natl. Acad. of Sci.* **2008**, *105*, 6813−6818.
30. Dash, P.K.; Moore, A.N.; Orsi, S.A. Blockade of γ−secretase activity within the hippocampus enhances long−term memory. *Biochem. Biophys. Res. Commun*. **2005**, *338*, 777−782.
31. Doig, A.J.; Derreumaux, P. Inhibition of protein aggregation and amyloid formation by small molecules. *Curr. Opin. Struct. Biol*. **2015**, *30*, 50−6.
32. Sánchez, Y.; Castillo, C.; Fuentealba, J.; Sáez–Orellana, F.; Burgos, C.F.; López, J.J.; F. de la Torre, A.; Jiménez, C.A. New benzodihydrofuran derivatives alter the amyloid β peptide aggregation: Strategies to develop new anti–alzheimer drugs. *ACS Chem. Neurosci*. **2023**, *14*, 2590–2602.
33. Hacker, R.M.; Smith, J.J.; Platt, D.C.; Brennessel, W.W.; Jones, M.A.; Webb, M.I. Ruthenium (II)–arene complexes with a 2, 2′−Bipyridine ligand as anti−Aβ agents. *Biomolecules* **2025**, *15*, 475.
34. Vyas, N.A.; Singh, S.B.; Kumbhar, A.S.; Ranade, D.S.; Walke, G.R.; Kulkarni, P.P.; Jani, V.; Sonavane, U.B.; Joshi, R.R.; Rapole, S. Acetylcholinesterase and Aβ aggregation inhibition by heterometallic ruthenium (II)–platinum (II) polypyridyl complexes. *Inorg. Chem.* **2018**, *57*, 7524−7535.
35. Wall, B.J.; Will, M.F.; Yawson, G.K.; Bothwell, P.J.; Platt, D.C.; Apuzzo, C.F.; Jones, M.A.; Ferrence, G.M.; Webb, M.I. Importance of hydrogen bonding: structure–activity

relationships of ruthenium (III) complexes with pyridine−based ligands for Alzheimer's disease therapy. *J. Med. Chem.* **2021**, *64*, 10124−10138.

36. Vyas, N.A.; Bhat, S.S.; Kumbhar, A.S.; Sonawane, U.B.; Jani, V.; Joshi, R.R.; Ramteke, S.N.; Kulkarni, P.P.; Joshi, B. Ruthenium (II) polypyridyl complex as inhibitor of acetylcholinesterase and Aβ aggregation. *Eur. J. Med. Chem.* **2014**, *75*, 375−381.
37. Chan, T.G.; Ruehl, C.L.; Morse, S.V.; Simon, M.; Rakers, V.; Watts, H.; Aprile, F.A.; Choi, J.J.; Vilar, R. Modulation of amyloid−β aggregation by metal complexes with a dual binding mode and their delivery across the blood–brain barrier using focused ultrasound. *Chem. Sci.* **2021**, *12*, 9485−9493.
38. Cendron, A.; Chianese, M.; Zarzycki, K.; Ruzza, P.; Honisch, C.; Brasuń, J.; Carraro, M. Chelating properties of N_6O−donors toward Cu (II) ions: Speciation in aqueous environments and catalytic activity of the dinuclear complexes. *Molecules* **2024**, *29*, 5708.
39. Wang, X.; Chan, H.N.; Desbois, N.; Gros, C.P.; Bolze, F.; Li, Y.; Li, H.W.; Wong, M.S. Multimodal theranostic cyanine−conjugated gadolinium (III) complex for *in viv*o imaging of amyloid−β in an Alzheimer's disease mouse model. *ACS Appl. Mater. Interfaces* **2021**, *13*, 18525−18532.
40. Cali, M.P.; Pereira, L.M.; Teodoro, M.D.; Sellani, T.A.; Rodrigues, E.G.; Carlos, R.M. Comparison of Aβ (1–40, 1–28, 11–22, and 29–40) aggregation processes and inhibition of toxic species generated in early stages of aggregation by a water−soluble ruthenium complex. *J. Inorg. Biochem.* **2021**, *215*, 111314.
41. Pasieka, A.; Panek, D.; Szałaj, N.; Espargaró, A.; Więckowska, A.; Malawska, B.; Sabaté, R.; Bajda, M. Dual inhibitors of amyloid–β and tau aggregation with amyloid–β disaggregating properties: Extended *in cellulo*, *in silico*, and kinetic studies of multifunctional anti–Alzheimer's agents. *ACS Chem. Neurosci.* **2021**, *12*, 2057–2068.
42. González–Sanmiguel, J.; Burgos, C.F.; Bascuñán, D.; Fernández–Pérez, E.J.; Riffo–Lepe, N.; Boopathi, S.; Fernández–Pérez, A.; Bobadilla–Azócar, C.; González, W.; Figueroa, M.; Vicente, B. Gabapentin inhibits multiple steps in the amyloid beta toxicity cascade. *ACS Chem. Neurosci.* **2020**, *11*, 3064−3076.
43. Dindar, Z.; Anbaraki, A.; Hosseini, S.S.; Harati, Z.; Bahrami, A.; Balalaie, S.; Ghobeh, M.; Mahdavi, M.; Seyedarabi, A. The use of natural volatile compounds on the fibrillation domain of amyloid beta (GSNKGAIIGLM) ─ towards promising agents to combat Alzheimer's disease. *ACS Chem. Neurosci*. **2025**, *16*, 1086−1102.
44. Zakaria, N.; Harun, W.M.R.S.W.; Latif, M.A.M.; Azaman, S.N.A.; Rahman, M.B.A.; Faujan, N.H. Effects of anthocyanidins on the conformational transition of $A\beta_{1-42}$ peptide: Insights from molecular docking and molecular dynamics simulations. *J. Mol. Graph. Model*. **2024**, *129*, 108732.
45. Nam, Y.; Prajapati, R.; Kim, S.; Shin, S.J.; Cheong, D.Y.; Park, Y.H.; Park, H.H.; Lim, D.; Yoon, Y.; Lee, G.; Jung, H.A. Dual regulatory effects of neferine on amyloid–β and tau aggregation studied by *in silico*, *in vitro*, and lab–on–a–chip technology. *Biomed. Pharmacother*. **2024**, *172*, 116226.

46. Dabas, A.; Goyal, B. Structural reorganization mechanism of the $A\beta_{42}$ fibril mediated by N–substituted oligopyrrolamide ADH–353. *ACS Chem. Neurosci.* **2024**, *15*, 3136−3151.

47. Mishra, C.B.; Shalini, S.; Gusain, S.; Kumar, P.; Kumari, S.; Choi, Y.S.; Kumari, J.; Moku, B.K.; Yadav, A.K.; Prakash, A.; Jeon, R. Multitarget action of benzothiazole–piperazine small hybrid molecule against Alzheimer's disease: *In silico*, *in vitro*, and *in vivo* investigation. *Biomed. Pharmacother.* **2024**, *174*, 116484.

48. Dabas, A.; Goyal, B. Delineating the tryptophan–galactosylamine conjugate mediated structural distortions in $A\beta_{42}$ protofibrils. *Phys. Chem. Phys.* **2025**, *27*, 7336−7355.

49. Peters, C.; Bascuñán, D.; Burgos, C.F.; Bobadilla, C.; González−Sanmiguel, J.; Boopathi, S.; Riffo, N.; Fernández−Pérez, E.J.; Tarnok, M.E.; Aguilar, L.F.; Gonzalez, W. Characterization of a new molecule capable of inhibiting several steps of the amyloid cascade in Alzheimer's disease. *Neurobiol. Dis.* **2020**, *141*, 104938.

50. Zardecki, C.; Dutta, S.; Goodsell, D.S.; Voigt, M.; Burley, S.K. RCSB: Protein data bank: A resource for chemical, biochemical, and structural explorations of large and small biomolecules. *J. Chem. Educ.* **2016.** *93*, 569−575.

51. Aliye, M.; Dekebo, A.; Tesso, H.; Abdo, T.; Eswaramoorthy, R.; Melaku, Y. Molecular docking analysis and evaluation of the antibacterial and antioxidant activities of the constituents of *Ocimum cufodontii*. *Sci. Rep.* **2021**, *11*, 10101.

52. Frisch, M. J.; Trucks, G. W.; Schlegel, H. B.; Scuseria, G. E.; Robb, M. A.; Cheeseman, J. R.; Scalmani, G.; Barone, V.; Petersson, G. A.; Nakatsuji, H.; Li, X.; Caricato, M.; Marenich, A.; Bloino, J.; Janesko, B. G.; Gomperts, R.; Mennucci, B.; Hratchian, H. P.; Ortiz, J. V.; Izmaylov, A. F.; Sonnenberg, J. L.; Williams−Young, D.; Ding, F.; Lipparini,F.; Egidi, F.; Goings, J.; Peng, B.; Petrone, A.; Henderson, T.; Ranasinghe, D.;Zakrzewski, V. G.; Gao, J.; Rega, N.; Zheng, G.; Liang, W.; Hada, M.; Ehara, M.; Toyota,K.; Fukuda, R.; Hasegawa, J.; Ishida, M.; Nakajima, T.; Honda, Y.; Kitao, O.; Nakai, H.Vreven, T.; Throssell, K.; Montgomery, Jr.; Peralta, J. E.; Ogliaro, F.; Bearpark, M.; Heyd, J. J.; Brothers, E.; Kudin, K.N.; Staroverov, V.N.; Keith, T.; Kobayashi, R.; Normand, J.; Raghavachari, K.; Rendell, A.; Burant, J.C.; Iyengar, S. S.; Tomasi, J.; Cossi, M.; Millam, J. M.; Klene, M.; Adamo, C.; Cammi, R.; Ochterski, J. W.; Martin, R. L.; Morokuma, K.; Farkas O., Foresman, J. B.; Fox, D. J. Gaussian 09, Revision A.02. *Gaussian, Inc., Wallingford CT*, **2016**.

53. Boopathi, S.; Kolandaivel, P. Fe^{2+} binding on amyloid β-peptide promotes aggregation. *Proteins* **2016**, *84*, 1257–1274.

54. DeLano W. L. The PyMOL molecular graphics system. **2002**, *571*, DeLano Scientific, San Carlos, CA.

55. Santoro, A.; Grimaldi, M.; Buonocore, M.; Stillitano, I.; D'Ursi, A.M. Exploring the early stages of the amyloid $A\beta_{1–42}$ peptide aggregation process: An NMR study. *Pharmaceuticals* **2021**, *14*, 732.

56. Malde K. A.; Zuo L.; Breeze M.; Stroet M.; Poger D.; Nair C. P.; Oostenbrink C.; E. A. Mark. An automated force field topology builder (ATB) and repository: Version 1.0. *J. Chem. Theory Comput.* **2011**, *7*, 4026−4037.

57. Briand, E.; Kohnke, B.; Kutzner, C.; Grubmüller, H. Constant pH simulation with FMM electrostatics in GROMACS.(A) Design and applications. *J. Chem. Theory Comput*. **2025**, *21*, 1762−1786.

58. Trott O.; Olson A. J. AutoDock Vina: Improving the speed and accuracy of docking with a new scoring function, efficient optimization and multithreading. *J. Comput. Chem.* **2010**, *31*, 455−461.

59. Li, J.; Feng, S.; Wang, X.; Zhang, B.; He, Q. Exploring the targets and molecular mechanisms of curcumin for the treatment of bladder cancer based on network pharmacology, molecular docking and molecular dynamics. *Mol. Biotechnol*. **2024**, 1−22.

60. Solis J. F.; Wets J.–B. R. Minimization by random search techniques. *Math. Oper. Res.* **1981**, *6*, 19−30.

61. Laskowski R. A.; Swindells M. B. LigPlot+: Multiple ligand–protein interaction diagrams for drug discovery. *J. Chem. Inf. Model.*, **2011**, *51*, 2778−2786.

62. (a) Van Der Spoel D.; Lindahl E.; Hess B.; Groenhof G.; Mark A. E.; Berendsen H. J. C. GROMACS: Fast, flexible, and free. *J. Comput. Chem.* **2005**, *26*, 1701−1718. (b) Abraham M. J.; Murtola T.; Schulz R.; Pall S.; Smith J. C.; Hess B.; E. Lindahl. GROMACS: High performance molecular simulations through multi–level parallelism from laptops to supercomputers. *SoftwareX* **2015**, *1*, 19−25.

63. (a) Qais, F.A.; Parveen, N.; Afzal, M.; Furkan, M.; Khan, R.H. Preventing amyloid–β oligomerization and aggregation with berberine: Investigating the mechanism of action through computational methods. *Int. J. Biol. Macromol.* **2024**, *258*, 128900. (b) Zakaria, N.; Harun, W.M.R.S.W.; Latif, M.A.M., Azaman; S.N.A., Rahman, M.B.A.; Faujan, N.H. Effects of anthocyanidins on the conformational transition of $A\beta_{1-42}$ peptide: Insights from molecular docking and molecular dynamics simulations. *J. Mol. Graph.* **2024**, *129*, 108732. (c) Mishra, C.B.; Shalini, S.; Gusain, S.; Kumar, P.; Kumari, S.; Choi, Y.S.; Kumari, J.; Moku, B.K.; Yadav, A.K.; Prakash, A.; Jeon, R. Multitarget action of benzothiazole–piperazine small hybrid molecule against Alzheimer's disease: *In silico*, *in vitro*, and *in vivo* investigation. *Biomed. Pharmacother.* **2024**, *174*, 116484.

64. Mark, P.; Nilsson, L. Structure and dynamics of the TIP3P, SPC, and SPC/E water models at 298 K. *J. Phys. Chem. A.* **2001**, *10*, 9954−9960.

65. Bussi G.; Donadio D.; Parrinello M. Canonical sampling through velocity rescaling. *J. Chem. Phys.* **2007**, *126*, 014101.

66. Parrinello M.; Rahman A. Polymorphic transitions in single crystals: A new molecular dynamics method. *J. Appl. Phys*. **1981**, *52*, 7182−7190.

67. Hess B.; Bekker H.; Berendsen H. J. C.; Fraaije J. G. E. M.; LINCS: A linear constraint solver for molecular simulations. *J. Comput. Chem.*, **1997**, *18*, 1463−1472.

68. (a) Essmann U.; Perera L.; Berkowitz M. L.; Darden T.; Lee H.; Pedersen L. G. A smooth particle mesh Ewald method. *J. Chem. Phys.*, **1995**, *103*, 8577−8593; (b) Darden T.; York D.; Pedersen L. Particle mesh Ewald: An $N\cdot\log(N)$ method for ewald sums in large systems. *J. Chem. Phys.* **1993**, *98*, 10089−10092.

69. Han, W.; Chen, Z.; Wang, M.W.; Zhou, Q. gmx_RRCS: A precision tool for detecting subtle conformational dynamics in molecular simulations. *J. Mo.l Bio.* **2025**, 169129.

70. Eisenhaber, F.; Lijnzaad, P.; Argos, P.; Sander, C.; Scharf, M. The double cubic lattice method: Efficient approaches to numerical integration of surface area and volume and to dot surface contouring of molecular assemblies. *J. comput. Chem.* **1995**, *16*, 273−284.

71. Hilt, S.; Rojalin, T.; Viitala, T.; Koivuniemi, A.; Bunker, A.; Wachsmann–Hogiu, S.; Kálai, T.; Hideg, K.; Yliperttula, M.; Voss, J.C. Oligomerization alters binding affinity between amyloid beta and a modulator of peptide aggregation. *J. Phys. Chem. C.* **2017**, *121*, 23974–23987.

72. Daura X.; Gademann K.; Jaun B.; Seebach D.; van Gunsteren W. F., Mark A. E. Peptide folding: When simulation meets experiment. *Angew. Chem. Int. Ed.* **1999**, *38*, 236−240.

73. Barot, P.A.; Maradiya, M.A.: Vora, J.J. Exploring the therapeutic potential of metal complexes of pregabalin and terbutaline: Spectroscopic insights and molecular docking in Alzheimer's and Parkinson's disease. *Orient. J. Chem.* **2024**, *40*.

74. Mohammed, A.A.; Barale, S.S.; Kamble, S.A.; Paymal, S.B.; Sonawane, K.D. Molecular insights into the inhibition of early stages of Aβ peptide aggregation and destabilization of Alzheimer's Aβ protofibril by dipeptide D−Trp−Aib: A molecular modelling approach. *Int. J. Biol. Macromol*. **2023,** *242*, 124880.

75. Inouye, H.; Gleason, K.A.; Zhang, D.; Decatur, S.M.; Kirschner, D.A. Differential effects of phe19 and phe20 on fibril formation by amyloidogenic peptide $A\beta_{16–22}$ (Ac-KLVFFAE-NH2). *Proteins: Struct. Funct. Bioinf.* **2010**, *78*, 2306–2321.

76. Kaur, R.; Narang, S.S.; Singh, P.; Goyal, B. Structural and molecular insights into tacrine–benzofuran hybrid induced inhibition of amyloid–β peptide aggregation and BACE1 activity. *J. Biomol. Struct. Dyn*. **2023**, *41*, 13211−13227.

77. Kaur, A.; Kaur, A.; Goyal, D.; Goyal, B. How does the mono–triazole derivative modulate $A\beta_{42}$ aggregation and disrupt a protofibril structure: Insights from molecular dynamics simulations. *ACS omega* **2020**, *5*, 15606–15619.

78. Singh, K.; Kaur, A.; Goyal, D.; Goyal, B. Mechanistic insights into the mitigation of Aβ aggregation and protofibril destabilization by ad−enantiomeric decapeptide rk10. *Phys. Chem. Chem. Phys.* **2022**, *24*, 21975−21994.

ak-msc-project-300625

ORIGINALITY REPORT

12%	3%	12%	1%
SIMILARITY INDEX	INTERNET SOURCES	PUBLICATIONS	STUDENT PAPERS

PRIMARY SOURCES

1	Apneet Kaur, Bhupesh Goyal. "Identification of new pentapeptides as potential inhibitors of amyloid–β42 aggregation using virtual screening and molecular dynamics simulations", Journal of Molecular Graphics and Modelling, 2023 Publication	2%
2	Submitted to Thapar University, Patiala Student Paper	1%
3	Kamaljot Singh, Anupamjeet Kaur, Deepti Goyal, Bhupesh Goyal. "Mechanistic insights into the mitigation of Aβ aggregation and protofibril destabilization by a D–enantiomeric decapeptide rk10", Physical Chemistry Chemical Physics, 2022 Publication	1%
4	Arushi Dabas, Bhupesh Goyal. " Delineating the tryptophan–galactosylamine conjugate mediated structural distortions in Aβ protofibrils ", Physical Chemistry Chemical Physics, 2025 Publication	1%
5	Amandeep Kaur, Anupamjeet Kaur, Deepti Goyal, Bhupesh Goyal. " How Does the Mono-Triazole Derivative Modulate Aβ Aggregation and Disrupt a Protofibril Structure: Insights from Molecular Dynamics Simulations ", ACS Omega, 2020 Publication	1%

Ajhish Kumar

Bhupesh Goyal
30/06/2025